




# JGR Solid Earth

## RESEARCH ARTICLE

10.1029/2024JB029787

# Depth Dependence of Coseismic Off-Fault Damage and Its Effects on Rupture Dynamics

Roxane Ferry<sup>1</sup> , Marion Y. Thomas<sup>2</sup> , Harsha S. Bhat<sup>3</sup> , and Pierpaolo Dubernet<sup>3</sup>

<sup>1</sup>Institute of Civil Engineering, Institute of Materials Science and Engineering, École Polytechnique Fédérale de Lausanne (EPFL), Lausanne, Switzerland, <sup>2</sup>Institut des Sciences de la Terre de Paris, Sorbonne Université, CNRS, UMR 7193, Paris, France, <sup>3</sup>Département de Géosciences, Laboratoire de Géologie, École Normale Supérieure, CNRS, UMR 8538, PSL Université, Paris, France

### Key Points:

- We use a mechanical model with a 1D fault to study how off-fault material changes and generated waves influence earthquake slip dynamics
- The off-fault damage zone narrows but becomes denser with depth, absorbing energy, stabilizing slip rates and reducing rupture velocity
- Interactions between bulk changes and fault slip drive both SSE and earthquake dynamics, emphasizing the importance of the whole fault zone

### Supporting Information:

Supporting Information may be found in the online version of this article.

### Correspondence to:

R. Ferry,  
roxane.ferry@epfl.ch;  
ferry.roxane@gmail.com

### Citation:

Ferry, R., Thomas, M. Y., Bhat, H. S., & Dubernet, P. (2025). Depth dependence of coseismic off-fault damage and its effects on rupture dynamics. *Journal of Geophysical Research: Solid Earth*, 130, e2024JB029787. <https://doi.org/10.1029/2024JB029787>

Received 25 JUN 2024

Accepted 5 FEB 2025

### Author Contributions:

**Conceptualization:** Roxane Ferry, Marion Y. Thomas, Harsha S. Bhat  
**Formal analysis:** Roxane Ferry, Marion Y. Thomas  
**Funding acquisition:** Marion Y. Thomas, Harsha S. Bhat  
**Investigation:** Roxane Ferry  
**Methodology:** Roxane Ferry, Marion Y. Thomas, Harsha S. Bhat  
**Resources:** Marion Y. Thomas, Harsha S. Bhat, Pierpaolo Dubernet  
**Software:** Roxane Ferry, Marion Y. Thomas, Harsha S. Bhat  
**Supervision:** Marion Y. Thomas, Harsha S. Bhat  
**Validation:** Roxane Ferry  
**Visualization:** Roxane Ferry, Marion Y. Thomas  
**Writing – original draft:** Roxane Ferry

**Abstract** Faults are complex systems embedded in an evolving medium fractured by seismic ruptures. This off-fault damage zone is shown to be thermo-hydro-mechano-chemically coupled to the main fault plane by a growing number of studies. Yet, off-fault medium is still, for the most part, modeled as a purely elastic—hence passive—medium. Using a micromechanical model that accounts for dynamic changes of elastic moduli and inelastic strains related to crack growth, we investigate the depth variation of dynamically triggered off-fault damage and its counter-impact on earthquake slip dynamics. We show that the damage zone, while narrowing with depth, also becomes denser and contrary to prevailing assumptions continues to act as an energy sink, significantly influencing rupture dynamics by stabilizing slip rates. Furthermore, we observe that damage formation markedly reduces rupture velocity and delays, or even prevents, the transition to supershear speeds even for a narrow damage zone. This underscores the critical need to incorporate the complex interplay between the main fault plane and its surrounding medium across the entire seismogenic zone. As a proof of concept, we introduce a 1D spring-slider model that captures bulk elastic variations, by modulating spring stiffness, and normal stress variations that emulate changes in bulk load. This simple model demonstrates the occurrence of slow slip events alongside conventional earthquakes, driven by the dynamic interaction between bulk temporal evolution and fault slip dynamics, without necessitating any changes to frictional properties.

**Plain Language Summary** Faults are part of a complex and evolving environment. Around these faults is a damaged rock area, known as the off-fault damage zone. Studies show this zone is interconnected with the main fault through thermal, hydraulic, mechanical, and chemical processes. However, most models treat the off-fault zone as purely elastic and passive medium. We use a model considering changes in material properties caused by cracking to understand how damage varies with depth and affects earthquake behavior. We find that the damage zone narrows but becomes denser with depth. Contrary to common beliefs, this zone continues to absorb energy, stabilizing the fault's motion during an earthquake. Our results show that damage generation slows down the rupture's speed and can prevent it from becoming supershear, even in narrow damage zones. This highlights the importance of considering interactions between the fault and its surrounding from the surface down to the end of the seismogenic zone. To extrapolate over the seismic cycle, we introduce a simple model simulating changes in surrounding material during fault slip. This model shows that both slow and fast earthquakes can occur due to dynamic interactions between the fault and the surrounding medium, without changing the fault's friction properties.

## 1. Introduction

Understanding on- and off-fault earthquake processes is crucial for effective mitigation of seismic hazard. To achieve this, comprehensive knowledge of fault zone physical properties and how it evolves through time and space is imperative.

Observations reveal that a real fault deviates significantly from the simplified conception of a planar fault embedded in an elastic medium. Faults exhibit roughness across various scales and are more appropriately referred to as fault systems. These systems encompass geometrical complexities ranging from the kilometric regional fault structure down to the smaller-scale fracture networks. At smaller scale, a fault structure is composed of a fault core abutted by a damage zone—a region characterized by intense fracturing due to fault slip—within the country rock. Based on field observations, damage density roughly decreases exponentially with distance from the fault (Mitchell & Faulkner, 2009) and induces changes in elastic properties (Pio Lucente et al., 2010; Qiu

**Writing – review & editing:**

Roxane Ferry, Marion Y. Thomas, Harsha S. Bhat

et al., 2021). Experimental evidences, such as the triaxial experiments conducted by Faulkner et al. (2006) and Mitchell and Faulkner (2012), demonstrates that Young's modulus decreases while Poisson's ratio and permeability rise with increasing damage. Additionally, along the Gofar transform fault, Froment et al. (2014) observed, after an earthquake, a drop in seismic velocities followed by a partial recovery and attributed it to coseismic-induced damage and subsequent healing mechanisms. A similar process has been observed by Brenguier et al. (2008) at Parkfield with a healing phase of approximately 3 years. This healing may entail microcrack closure due to stress alterations or fracture sealing driven by chemical processes (Brantut et al., 2013; Mitchell & Faulkner, 2008). Finally, a decrease in the damage zone width with depth has been observed both in field study (Cochran et al., 2009) and inferred from numerical simulations (Okubo et al., 2019).

Numerous studies have recently highlighted the strong thermo-hydro-mechano-chemical (THMC) coupling that exists between faults and their surrounding environments. For example, geometrical complexity exerts a strong influence on the seismicity (Barnes et al., 2020; Bedford et al., 2022; Mia, Abdelmeguid, et al., 2024; Morad et al., 2022; Palgunadi et al., 2024; Xu et al., 2023). The numerical study by Romanet et al. (2018) demonstrated that slow slip events (SSEs) and regular earthquakes emerge at the same location from a simple two overlapping faults system with spatially constant rate-and-state parameters, showing that fault geometrical complexity induces complex slip dynamics. In their analysis of 27 earthquakes, Perrin et al. (2016) concluded that the degree of fault damage correlates with the amount of slip during an earthquake. When a fault slips the off-fault damage induces a change in bulk physical properties which in turn significantly affects the fault behavior. Damage-induced changes in elastic properties not only alter rupture extension and dynamics (e.g., Thomas et al., 2017, and others), but also influence permeability, leading to changes in pore pressure that subsequently affect the fault's resistance to slip. In their study of the Gofar transform fault, Froment et al. (2014) demonstrated a covariation between seismicity rates and changes in seismic velocity over time due to healing processes. Additionally, the evolution of the bulk medium plays a crucial role in the stored energy within it. The damage zone, for instance, can serve as an energy sink for off-fault energy dissipation (Andrews, 2005; Johnson et al., 2021). Furthermore, contrary to previous beliefs, recent modeling by Okubo et al. (2020) revealed that the damage zone significantly contributes to the overall energy budget, even at depths where its width narrows but crack density increases. Finally, time evolution of bulk properties can affect the mode of slip, as we further demonstrate in this paper.

Although numerous geological, geodetical and numerical studies have highlighted the coupling between the bulk and the fault plane, they are still studied as independent entities. Prevailing modeling strategies typically assume that the effects of the damage zone can be disregarded, particularly as it narrows with depth. However, the objective of this study is to challenge this assumption by examining the significance of the damage zone and its impact on rupture dynamics, even in regions where it is narrower. In the initial section, we introduce the damage model characteristics and parametrization. In the second section, we explore the evolution of damage zone characteristics with increasing depth. The third section is dedicated to examining the influence of the damage zone on the dynamics of rupture. Finally, we introduce in the discussion a simplified “proof of concept” model that integrates a secondary cycle along the traditional seismic cycle, to discuss how the dynamic evolution of fault zone properties with slip behavior can impact the deformation modes. This approach highlights the importance of taking into account the fault zone structure inheritance into the seismic cycle. It emphasizes the necessity to account for the evolving properties of both the fault core and the surrounding bulk material, underscoring their complex interplay and significance for seismic hazard assessment and mitigation strategies.

## 2. Materials and Methods

The damage zone as a function of depth is studied using a constitutive damage model implemented in the 2D fully dynamic spectral element code SEM2DPACK (Ampuero, 2012). The micromechanical model used in this study accounts for dynamic evolution of elastic moduli at high-strain rates and includes a physical crack-growth law to model the evolution of damage. This enables the modeling of the feedback between off-fault damage and seismic rupture. The model uses an energy-based approach to determine the nonlinear constitutive strain-stress relationship of a damaged solid. In other words, fracture damage is accounted for by creating an energetically equivalent solid. Below only key characteristics of the model are presented, but a more detailed description can be found in Bhat et al. (2012) or Thomas and Bhat (2018).

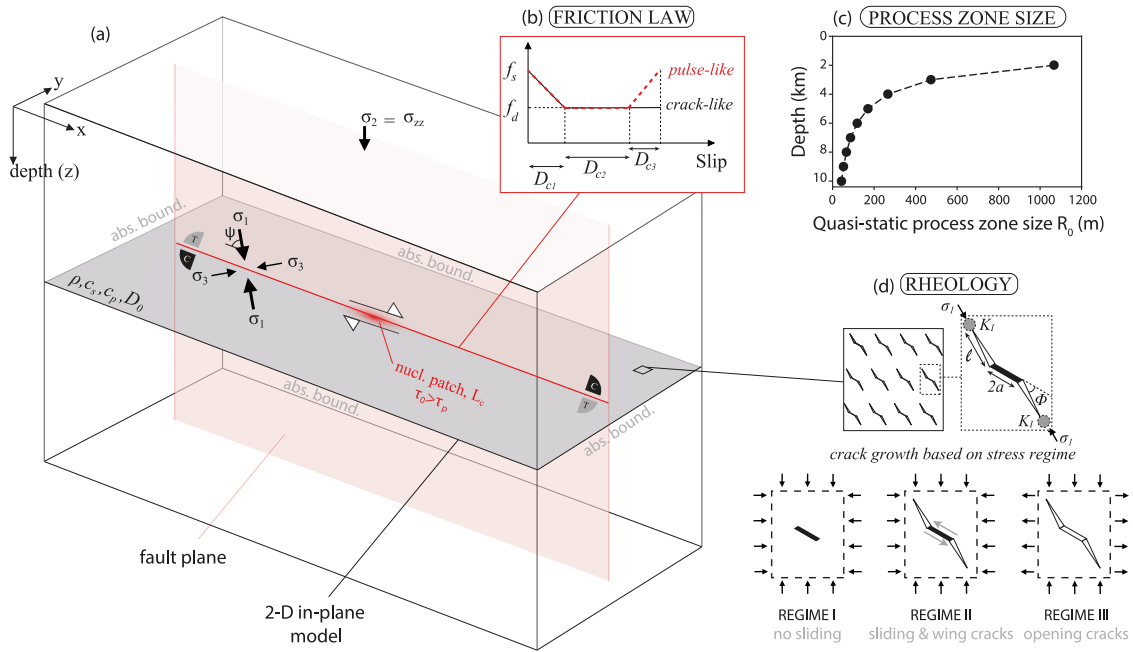


**Figure 1.** (a) Schematic 3D model: 1D projection (red line) of a 2D strike-slip fault (salmon) onto a 2D in-plane model (gray). The fault is governed by a slip weakening restrengthening friction law.  $T$  and  $C$  denotes tensional and compressional quadrants, respectively. (b) Slip-weakening-restrengthening law used (red). (c) Quasi-static process zone size  $R_0$  as a function of depth. (d) Regimes for inelastic deformation.

### 2.1. Constitutive Laws for Damage Modeling

Figure 1 presents the model overview. The medium surrounding fault is represented as an isotropic elastic solid containing pre-existing monosized flaws in the form of penny-shaped cracks of radius  $a$  with a volume density  $N_v$  remaining constant which implies no nucleation of new cracks. Only cracks optimally oriented from a Coulomb friction perspective are considered, meaning cracks aligned to  $\sigma_1$  at the angle  $\Phi = \frac{1}{2} \tan^{-1}(1/f_c)$ , where  $f_c$  is the friction coefficient and  $\sigma_1$  is the largest stress component. The initial damage state  $D_0$ , representing the density of initial flaws per unit volume, is given by:

$$D_0 = \frac{4\pi}{3} N_v (a \cos \Phi)^3, \quad (1)$$

with  $a \cos \Phi$  the projection of the crack radius on  $\sigma_1$ .

In the model, inelastic deformation occurs through the opening and/or propagation of pre-existing cracks. These cracks grow parallel to  $\sigma_1$  in the form of tensile wing-cracks of length  $l$  that nucleate at the tips of the penny-shaped flaws. Consequently, the current damage state, representing the fraction of volume occupied by micro-cracks and reflecting the inelastic state of the solid is:

$$D = \frac{4\pi}{3} N_v (a \cos \Phi + l)^3. \quad (2)$$

Here,  $D \in [D_0, 1]$ , with  $D = 1$  indicating the coalescence stage that leads to the macroscopic failure of the solid. The damage state increases as cracks grow following a state evolution law derived by differentiating Equation 2 with respect to time:

$$\frac{dD}{dt} = \left( \frac{3D^{2/3} D_0^{1/3}}{a \cos \Phi} \right) \frac{dl}{dt}, \quad (3)$$

with  $dl/dt$  the instantaneous wing-crack tip speed.

At each time step, depending on the local state of stress within a cell of the simulated domain, three different regimes can be reached (Figure 1d). Under compressive loading Regime I, stresses are not sufficiently high to induce sliding along microcracks and the solid behaves like an isotropic linear elastic material. Still for compressive loading, Regime II is reached when the shear stress  $\tau$  overcomes the frictional resistance  $f_c(-\sigma_n)$  acting on microcracks, with  $\sigma_n$  the normal stress. In this regime, inelastic deformation is accounted for by the growth of tensile wing cracks at the tip of the penny-shaped cracks. Under tensile loading Regime III, both penny-shaped cracks and wing-cracks can open.

Crack growth depends on both the local stress conditions at the crack tip and the material's ability to resist fracture. In the model, a crack grows if the dynamic microcrack stress intensity factor  $K_I^d$  overcomes the material resistance to fracturing, given by the material dynamic initiation toughness  $K_{IC}^D$  ( $K_I^d \geq K_{IC}^D$ ). Once the crack is initiated, the crack growth is controlled by the dynamic propagation toughness  $K_{IC}^d$ . Then we obtain from the above-mentioned a nonlinear equation for the crack-tip speed  $dl/dt$  that can be used in Equation 3 to solve for damage evolution. Experiments have shown that fracture toughness of rock is rate dependent. Therefore, under high loading rates approaching coseismic conditions, it is more difficult to initiate and propagate cracks (Gao et al., 2015; Wang et al., 2011; Zhang & Zhao, 2013). This rate dependency of fracture toughness represents the key ingredient of this damage model, compare to other micromechanical models.

Following the formalism of equilibrium thermodynamics and leveraging the properties of thermodynamic potential, we recomputed the homogenized constitutive relationship between stress and strain and its evolution by the state variable  $D$  defined in Equation 2 (Rice, 1971). A detailed description of the model is provided in the supplementary material of Thomas and Bhat (2018).

## 2.2. Non-Dimensionalization

The system is non-dimensionalized by the quasi-static process zone size  $R_0$  which characterizes the length scale of the frictional weakening process (and hence provides a guideline for numerical resolution) (Poliakov et al., 2002; Rice et al., 2005). It is given by:

$$R_0(z) = \frac{9\pi\mu G}{16(1-\nu)[(f_s - f_a)(-\sigma_{yy}^0(z))]^2}, \quad (4)$$

with  $\mu$  the shear modulus,  $G$  the fracture energy,  $\nu$  the Poisson's ratio and  $\sigma_{yy}^0$  the initial stress normal to the fault.

Therefore, the grid size depends on  $R_0$  to maintain a consistent process zone resolution for simulations at different depths. As  $R_0$  decreases with depth (Figure 1c) as a function of  $\sigma_{yy}^0(z)^{-2}$ , the grid size also decreases. In all simulations the process zone is resolved using 20 nodes. Figure S1 in Supporting Information S1 highlights the importance of non-dimensionalization.

The time step  $\Delta t$  is chosen according to a Courant–Friedrichs–Levy (CFL) condition:  $\Delta t = C\Delta x/c_p$ , where  $C$  is the CFL constant,  $\Delta x$  the grid size and  $c_p$  the longitudinal wave speed. Between simulations at various depths, the sole parameter modified is the grid size  $\Delta x$  which linearly depends on  $R_0$ . Therefore, the time step is inherently dependent on the parameter  $R_0$ .

## 2.3. Numerical Method and Model Set Up

We consider a 2D in-plane model (gray plane in Figure 1a) with a 1D right-lateral fault (red line) at a prescribed depth. Rupture is promoted using a nucleation prone patch in the middle of the fault where the initial shear stress is slightly above the fault strength (0.01%). The length of this patch is taken to be 10% above the minimum nucleation length  $L_{nuc}$  defines as (Palmer et al., 1973):

$$L_{nuc} = \frac{64}{9\pi^2}(1+S)R_0, \quad (5)$$

where the parameter  $S = (\tau_p - \tau_0)/(\tau_0 - \tau_r)$ , as defined by Andrews (1976), gives the threshold at which seismic rupture becomes supershear ( $S < 1.77$ ). The terms  $\tau_p = -f_s\sigma_{yy}$  and  $\tau_r = -f_d\sigma_{yy}$  are the peak and residual strengths, respectively, and  $\tau_0$  is the initial shear stress.

We use a slip-weakening law with restrengthening (Figure 1b) to generate a pulse-like rupture. As a consequence, over the slip distance  $D_{c2}$ , the fault strength increases up to its static value preventing the fault to slip further. Thus, even as the rupture propagates, only a small portion of the fault is sliding at a given time. This allows for a fair comparison between simulations by avoiding the effect of having different rupture durations. This distance is directly proportional to  $D_{c1}$  which varies with depth, or more precisely with  $\sigma_{yy}$  (see Jeandet Ribes et al. (2023) for its relation to depth) as:

$$D_{c1} = \frac{2G}{(f_s - f_d)(-\sigma_{yy}(z))}. \quad (6)$$

where  $G$ , the fracture energy required to break the contact connection (Palmer et al., 1973), is assumed to remain constant with depth.

Uniform background stresses are applied with the maximum compressive stress  $\sigma_1$  forming a  $60^\circ$  angle with the fault plane. The initial normal and shear stresses are uniform along the fault, except for the nucleation patch. 2D simulations are performed under the plane-strain assumption but the initial stress field is set up in 3D to ensure a correct stress field as emphasized by Jeandet Ribes et al. (2023). Under the plane-strain assumption, the initial stress state is given by:

$$\sigma_{ij}^0 = \begin{pmatrix} \sigma_{xx}^0 & \sigma_{xy}^0 & 0 \\ \sigma_{xy}^0 & \sigma_{yy}^0 & 0 \\ 0 & 0 & \sigma_{zz}^0 \end{pmatrix}. \quad (7)$$

Assuming a parameter  $S$  and the friction coefficients  $f_s$  and  $f_d$ , one can get the initial friction  $f_0$ :

$$f_0 = \frac{f_s + Sf_d}{1 + S} = \frac{\sigma_{xy}^0}{-\sigma_{yy}^0}. \quad (8)$$

The vertical stress  $\sigma_{zz}^0$  depends linearly on depth following:

$$\sigma_{zz}^0 = \rho gz(1 - \lambda), \quad (9)$$

with  $\rho$  the density of rock,  $g$  the gravitational acceleration,  $z$  the depth measured from the surface and  $\lambda$  the pore pressure ratio. We assume a constant  $\lambda$  with depth although this may not hold true due to a potential transition from hydrostatic to lithostatic conditions. Such a transition could influence the damage zone width and requires more careful investigation. However, in this model, we aim to minimize the number of parameters. Additionally,  $\sigma_{zz} = \nu(\sigma_{xx} + \sigma_{yy})$ . Assuming an angle  $\Psi$  between the most compressive stress  $\sigma_1$  and the fault plane, the following equality holds:

$$\frac{2f_0}{\tan(2\Psi)} + 1 = \frac{\sigma_{xx}^0}{\sigma_{yy}^0}. \quad (10)$$

This allows to derive the last stress matrix components:

$$\sigma_{yy}^0 = \frac{\sigma_{zz}^0}{\nu\left(\frac{2f_0}{\tan(2\Psi)} + 2\right)}, \quad (11a)$$

**Table 1**  
Bulk Static Friction Coefficient at Each Studied Depth

Depth (km)	Bulk static friction coefficient
2	0.84
3	0.78
4	0.75
5	0.73
6	0.72
7	0.71
8	0.71
9	0.70
10	0.70

depth as shown in Section 2.2, and on the friction coefficient on the microcracks,  $f_c$ . Consequently,  $f_c$  varies with depth while adhering to experimental values ( $f_c \in [0.7, 0.84]$ , see Table 1). It is important to note that we do not assert that the static friction coefficient naturally varies with depth. Instead, our objective is to facilitate a fair comparison by isolating the influence of depth on the generation of the damage zone.

All parameters values used are given in Table 2.

### 3. Evolution of Damage Zone Width and Density With Depth

To explore the evolution of damage zone width and density with depth, simulations were conducted at 1 km depth intervals ranging from 2 to 10 km. Figure 2 depicts the damage state at the end of each simulation for the respective depths. Given the symmetry of the rupture with respect to the fault center, only one quarter of the domain is presented except for the simulation at 2 km depth.

At a first glance, the damage states at different depth look similar: they all develop highly damaged elongated branches with  $D$  close to 1 and a maximum length of approximately  $2.5 R_0$ , making an angle of  $\approx 60 - 70^\circ$  which

is close to  $\Psi$ . However, as  $R_0$  decreases drastically with depth (Figure 1c), there is a corresponding diminution in the extent of the damage zone. The left panel of Figure 3 shows the evolution of the maximum damage zone width with depth, defined as the furthest distance from the fault at which  $D \geq D_{thres}$ . Notably, regardless of the chosen  $D_{thres}$ , the evolution of the damage zone width with depth reveals a funnel-shaped structure. Note that to prevent potential confusion with a term employed in tectonics to denote a particular architecture of strike-slip systems, we have opted not to employ the term “flower structure” despite its occasional usage in the literature. We instead humbly suggest “funnel-shaped structure.” This structure aligns well with geophysical observations of Cochran et al. (2009) and is consistent with the findings from simulations conducted by Okubo et al. (2019). Their approach to model damage differs from ours: coseismic off-fault damage is accounted for with nucleation of new cracks but elastic properties are kept constant. In our approach there is no nucleation of new cracks, but damage is accounted for by computing the change in elastic properties due to crack growth. Each method has its own strengths and limitations. In solid mechanics, the distinction between these approaches is well-defined. However, in earthquake physics, physical processes occur across a wide range of scales, necessitating both explicit and implicit characterizations of dissipation phenomena. Ideally, a robust method for dynamically modeling damage would integrate small- and large-scale fracture formation while accounting for elastic moduli changes (at both fine and large scales) in the medium to properly model the intricate feedbacks between the off-fault damage generation and the dynamic

**Table 2**  
Parameters Used for Simulations With SEM2DPAK

Symbol	Parameter	Value
$\mu$	Shear modulus	26.2 GPa
$\nu$	Poisson's ratio	0.276
$\rho$	Density of rock	2700 kg/m <sup>3</sup>
$\Psi$	Orientation of $\sigma_1$	60°
$S$	Seismic ratio	1
$\lambda$	Lithostatic pore pressure	0.4
$f_c$	Bulk friction coefficient	[0.7, 0.84]
$f_s$	Fault static friction coefficient	0.6
$f_d$	Fault dynamic friction coefficient	0.1
$D_c$	Critical slip distance	from Equation 6
$D_{c2}$	Critical slip distance 2	$5 \times D_{c1}$
$D_{c3}$	Critical slip distance 3	$0.1 \times D_{c1}$
$G$	Fracture energy	$\approx 22$ MJ/m <sup>2</sup>
$D_0$	Initial damage state	0.1
$c_s$	S-wave speed	3,115 m/s
$c_p$	P-wave speed	5,600 m/s

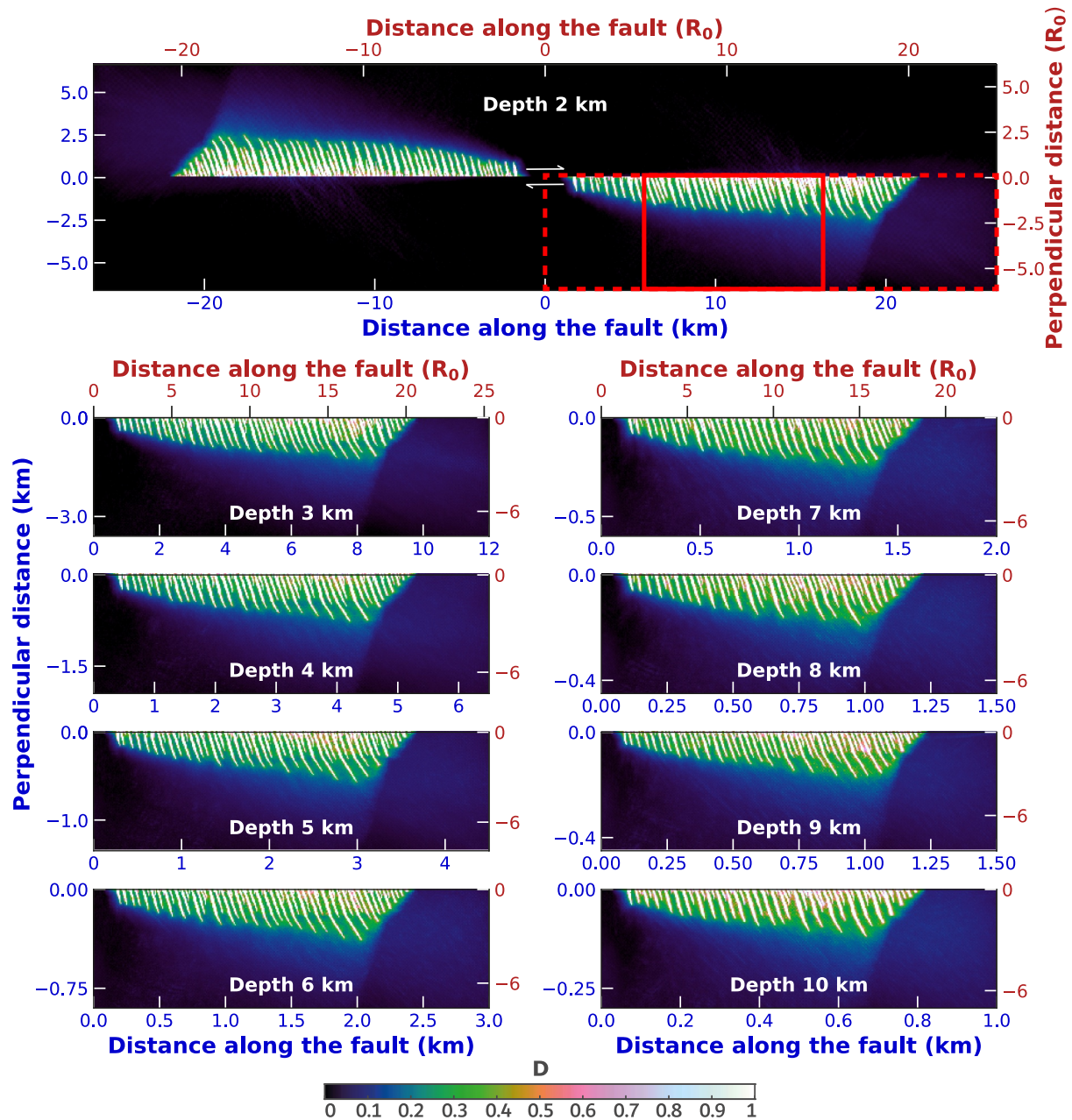


**Figure 2.** Comparison of damage arising from a rupture at depths ranging from 2 to 10 km. The top panel depicts the entire fault at a depth of 2 km. The small red rectangle demarcates the region from which densities in Figure 3 are computed. Given the symmetry of the rupture, the subsequent panels exclusively showcase the bottom-right quadrants (as delimited by the dashed red rectangle in the top panel) of the domain. Both real (km) and non-dimensionalized ( $R_0$ ) distances are given.

rupture. Unfortunately, such a method is not yet available. Our aim is to show that a funnel-shaped structure, consistent with geophysical observations, emerges in both end-members models (Okubo et al. (2019) and ours). This convergence supports the idea that the observed structure aligns with natural geological formations.

In the right panel of Figure 3, we compare the average damage states with perpendicular distance from the fault at depths of 2, 6, and 10 km. Bright colors represent the average damage state, while shaded areas indicate standard deviation. It is clear that, away from the fault, at distances higher than  $\approx 2.5 R_0$ , a distance that aligns with the size of the branches, the damage density increases with depth. Regions closer to the fault exhibit a more ambiguous trend; however, within this region, the value of the standard deviation increases with depth, indicating a higher

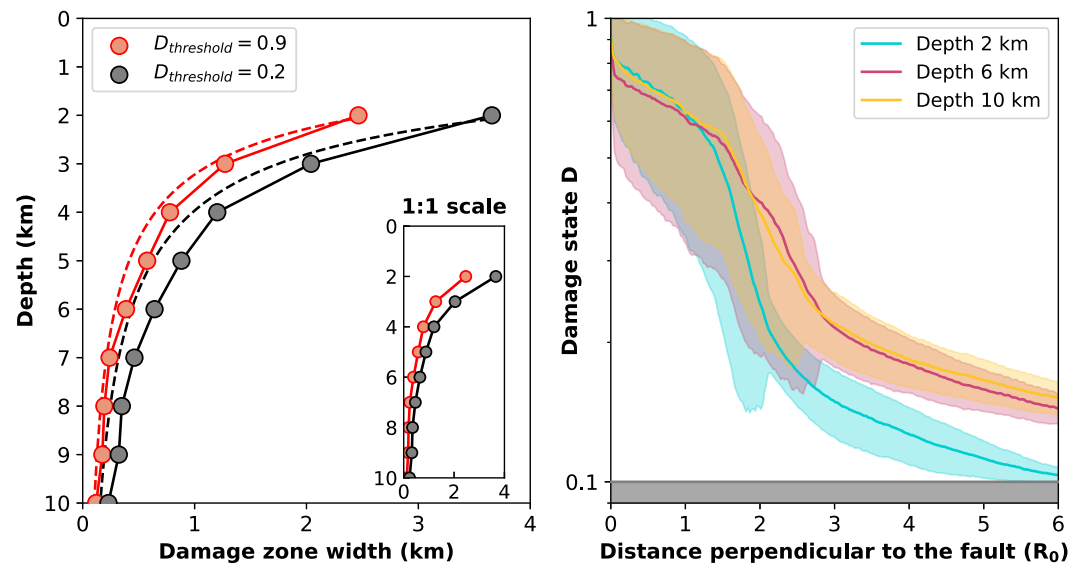


**Figure 3.** Left: Damage zone width as a function of depth for two distinct damage thresholds, revealing a consistent funnel-shaped structure. The dashed lines indicate a fit by  $c R_0$ , with  $c$  a positive constant ( $\approx 2.3$  and  $3.4$  for the threshold  $0.9$  and  $0.2$ , respectively). The inset displays the same scale for both width and depth. Right: Comparison of damage density with perpendicular distance from the fault for simulations at 2, 6, and 10 km depth. Computations are done in a region between 10 and  $15 R_0$  away from the fault center to avoid nucleation effects. The location is shown in Figure 2 as a red rectangle. Bright colors represent the average damage state for a given distance perpendicular to the fault, while shaded areas indicate the standard deviation. The gray area marks the initial damage state  $D = 0.1$ . Note the logarithmic scale for the damage state.

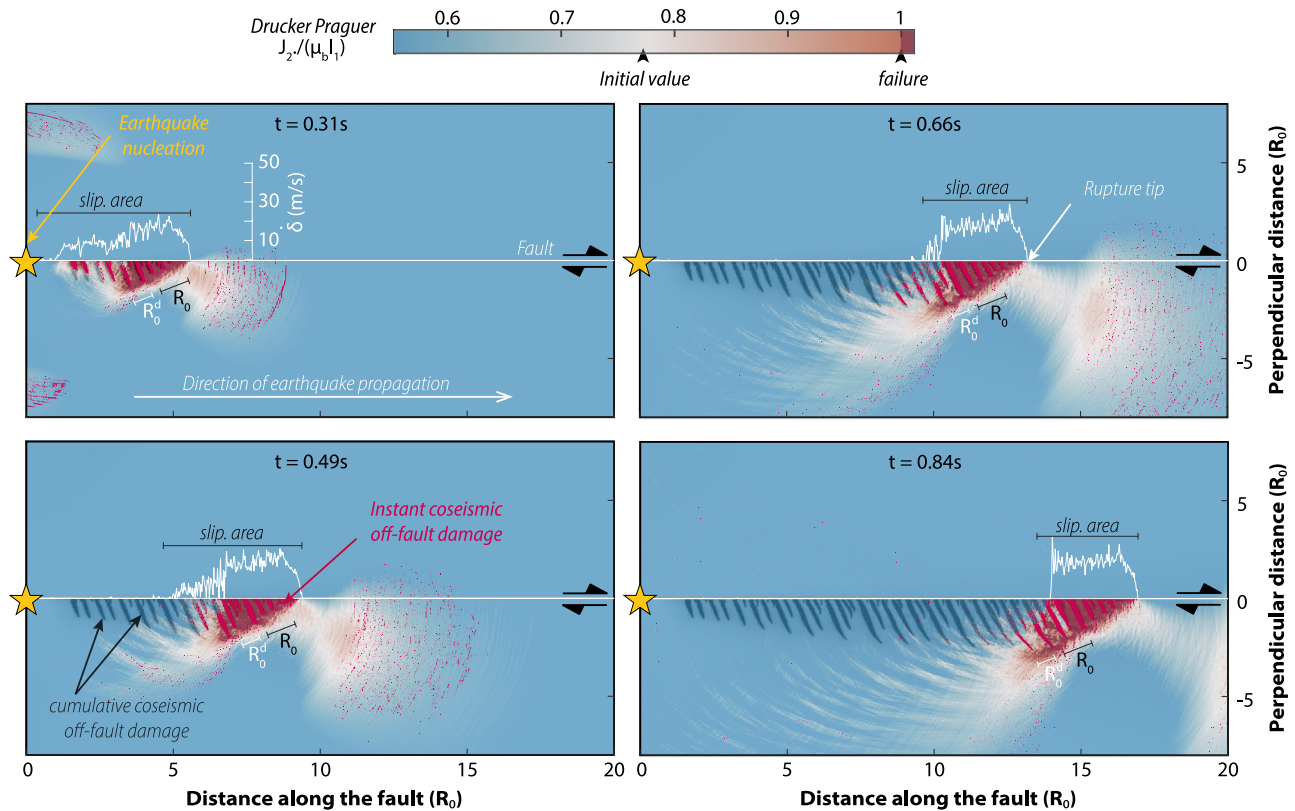
overall damage state. The diminished distinction closer to the fault can be attributed to the saturation of the damage state  $D$  to 1, a limitation inherent to our model.

Figure 4 illustrates the rupture propagation at a specific reference depth of 6 km. The Drucker-Prager yield criterion in the background delineates areas where coseismic off-fault damage predominantly occurs. Additionally, the graph displays the fault slip rate (in white) at the time of the snapshot, cumulative damage (in gray) accumulated so far, and off-fault damage during this particular time step (in red). Coseismic off-fault damage primarily occurs behind the rupture front, where the fault slip. The damage occurring behind the area which is currently slipping is a result of cascading effects associated with the growth of these branches, altering the stress state ahead of them. Propagating waves in the medium are also playing a role. Notably, the spacing between branches seems to correspond primarily to the dynamic process zone size, reflecting the intricacies of the dynamic rupture process.

The elongated branches observed herein manifest as a consequence of a single rupture within a medium characterized by a homogeneous initial damage state. This contrasts with field observations, where the signature of multiple ruptures persists. They show an exponential (Faulkner et al., 2006, 2011; Mitchell & Faulkner, 2009; Vermilye & Scholz, 1998; Wilson et al., 2003) or power law (Rodríguez Padilla et al., 2022; Savage & Brodsky, 2011) decay in the damage state with increasing distance from the fault. Consequently, we chose to run additional simulations with an initial damage state decreasing exponentially from  $D_0 = 0.6$  to  $D_0 = 0.1$  over a distance  $3 R_0$ . Figure S2 in Supporting Information S1 shows the corresponding damage state at the end of each simulation for the respective depths. The damage zones exhibit comprehensive regions characterized by heightened damage, as opposed to isolated branches in the case of an homogeneous initial damage state. Even in this case, the evolution of the maximum damage zone width with depth has a funnel-shaped structure as shown in Figure S3 in Supporting Information S1.

For both an homogeneous initial damage stage and an exponentially decreasing one, the damage zone narrows with depth in correlation with the reduction of the process zone size. Despite the relatively small width of the damage zone, its influence on rupture dynamics remains significant, given that all processes occur at the scale of the process zone. The next section aims to illustrate the damage zone influence on rupture dynamics.





**Figure 4.** Temporal evolution of a dynamic rupture at 6 km depth. Colors indicate the normalized Drucker-Prager yield criterion as reference. Fault slip rates (white curves) highlight the slipping area, and cumulative damage  $D$  (gray scale) is superimposed. Instantaneous coseismic off-fault damage is underlined in red. The static and dynamic process zone sizes  $R_0$  and  $R_0^d$  are indicated.  $R_0^d$  is numerically calculated as the distance behind the crack tip where the slip is equal to  $D_{c1}(z)$ . The yellow star denotes the nucleation patch.

#### 4. Damage Influence on Rupture Dynamics

Figure 5 compares the cumulative slip and the slip rate for the elastic and damage cases at 6 km depth. In the elastic scenario, the slip rate keeps growing as slip accumulate, as predicted theoretically for the law we are using. However, in the presence of damage, the slip rate remains approximately constant, effectively mitigating the emergence of nonphysical singularities in the slip rate. The oscillations observed in the slip rate for the damage case are attributed to the generation of high-frequency waves (Thomas et al., 2017). The cumulative slip illustrates in both cases the pulse-like nature of the rupture consistent with the employed slip-weakening-restrengthening law. The shaded dark and light gray regions highlight the slipping portion of the fault during the same time interval for the damage and elastic cases, respectively, showing a broader pulse width for the elastic case. This is related to the fact that the ruptures become supershear for the purely elastic cases (for a more detailed discussion, please refer below). These findings persist across all depths as shown in Figures S4 and S5 in Supporting Information S1. For both the damage and elastic cases, the slip rate increases with depth.

Figure 6a compares the evolution of rupture front locations over time at 2, 4, 6, and 10 km depth for both elastic and damage cases. In the damage scenarios, rupture speeds remain approximately constant and are consistently lower than those observed in the corresponding elastic cases: damage generation slows the rupture speed at all depths. In the elastic case, the rupture swiftly transitions to supershear as highlighted, while in the damage case, it consistently remains within the subshear domain. Damage generation thus delays, if not entirely prevents, the transition to supershear at all depths in these cases. Therefore, the existence of a damage zone could explain why supershear ruptures are not as ubiquitous in nature. It is worth pointing that Thomas and Bhat (2018) observed a supershear transition in the presence of damage using the same model but under different settings on a smaller fault. Understanding the role of damage in the supershear transition will therefore necessitate further studies. It is

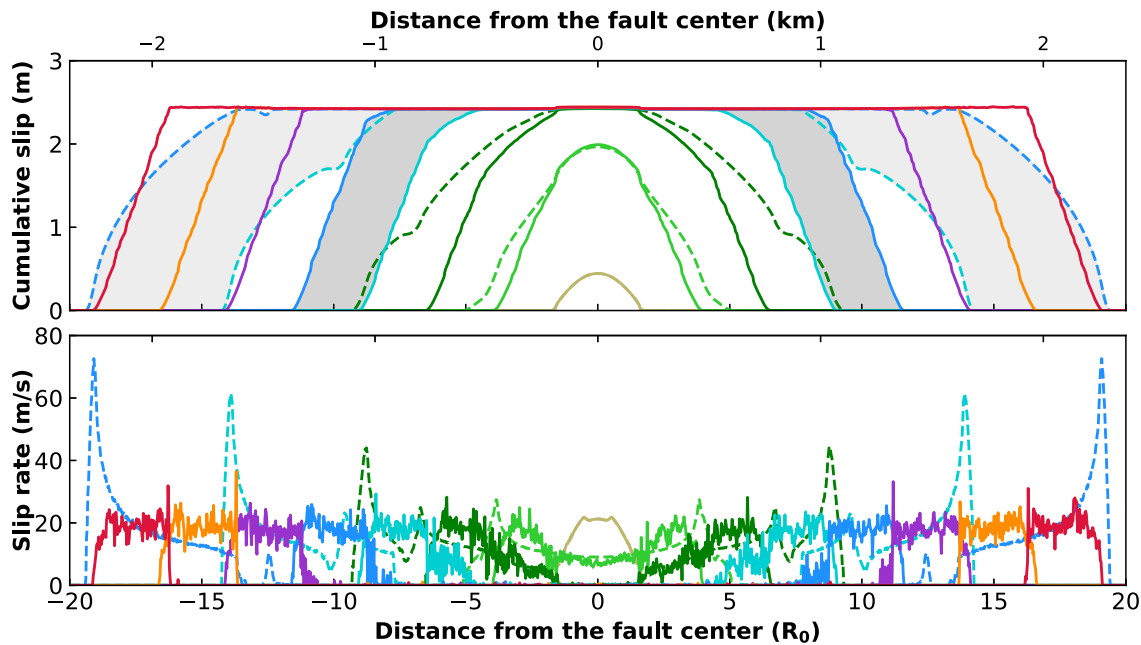


**Figure 5.** Comparison of cumulative slip (top) and slip rate (bottom) as a function of distance from the fault center for both the elastic (dashed lines) and damage (continuous lines) cases at 6 km depth. Colors are isochrones, the dark and light gray areas highlight the area that slipped during a given time interval for the damage and elastic case respectively. Both real (km) and non-dimensionalized ( $R_0$ ) distances are given.

noteworthy that in our case this transition to supershear occurs at the same non-dimensionalized time across all depths, suggesting a dependence on the process zone size.

The peak velocities over time (Figure 6b) increase with depth for both elastic and damage scenarios. For the damage cases, these peaks remains relatively constant over time at a given depth. The oscillations in the peak velocities are attributed to the off-fault related high-frequency content (see Figure 7 for a discussion). With an initial damage state decreasing exponentially, the damage preceding the rupture front exceeds that observed in the initial homogeneous damage case, resulting in a further deceleration of the rupture front (Figure S6a in

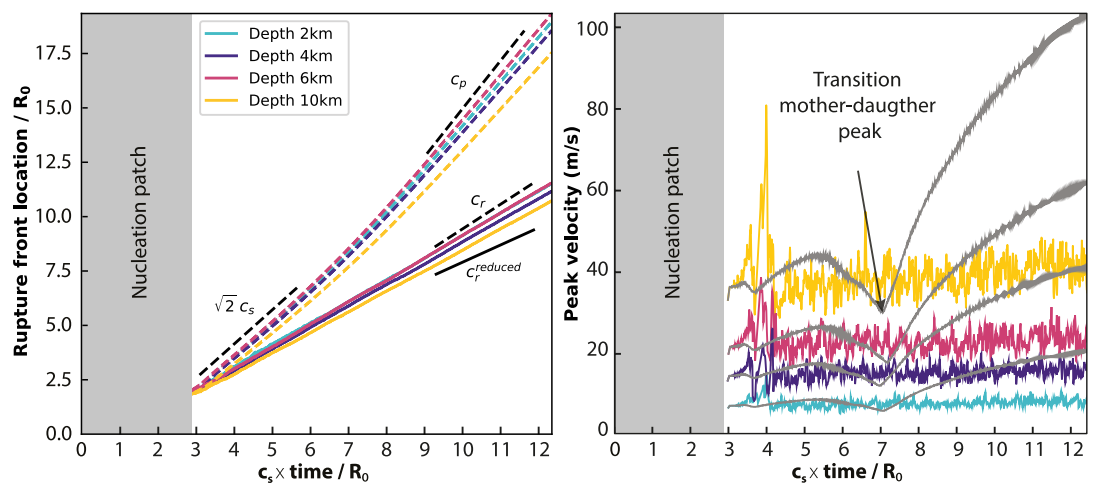


**Figure 6.** Left: Comparison of rupture front locations as a function of dimensionless time at different depths both for elastic (dashed lines) and damage (continuous lines) cases. The black dashed lines indicate for reference the speed domain limits for stable supershear rupture,  $\sqrt{2}c_s$  and  $c_p$ , as well as the upper limit for subshear rupture  $c_r$ , where  $c_s$ ,  $c_p$  and  $c_r$  are respectively the shear, longitudinal and Rayleigh wave speeds. The continuous black line illustrates the reduced Rayleigh wave speed (decreased by 30%) due to damage. Right: Comparison of peak velocity in  $m/s$  as a function of dimensionless time at different depths both for elastic (dashed gray lines) and damage (continuous lines) cases.

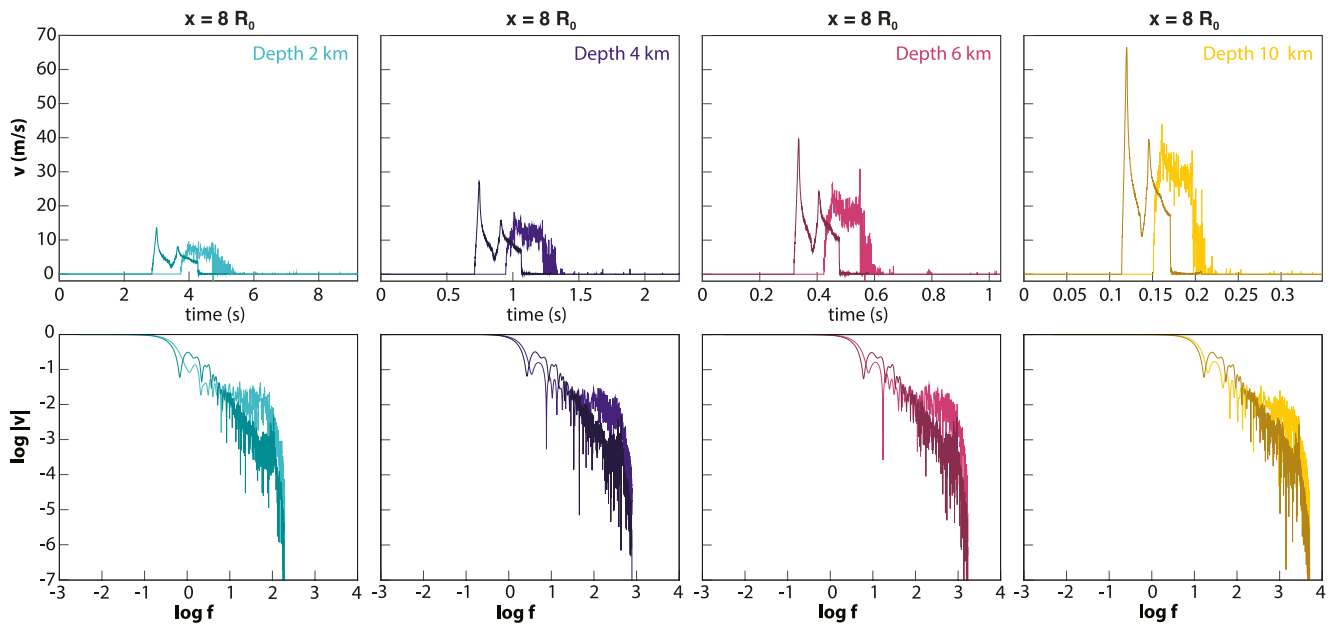


**Figure 7.** Comparison of Fourier amplitude spectra (FAS) of slip rate at different depths. The dark and light colors correspond to the elastic and damage case, respectively.

Supporting Information S1). Conversely, in comparison to the homogeneous case, we note an escalation in peak velocity (Figure S6b in Supporting Information S1) along with a reduction in oscillations. This observation is linked to the nature of the newly formed damage zone, which exhibits greater homogeneity.

Figure 7 compares the Fourier amplitude spectra (FAS) of slip rate at various depths. Across all depths, the slip rate in the damage case exhibits a higher-frequency content than in the elastic case, as evidenced by a steeper slope in the Fourier velocity spectra beyond a specific frequency threshold. This phenomenon is primarily attributed to alterations in elastic properties caused by damage, culminating in the formation of a Low-Velocity Zone (LVZ) characterized by up to a 30% decrease in wave speed. The resulting contrast in material properties leads to internal wave reflections that interact with the propagating rupture, producing a high-frequency content. The generated damage also radiates waves, a phenomenon observable upon closer examination of the created branches (Ben-Zion & Ampuero, 2009; Thomas & Bhat, 2018). This analysis is in agreement with laboratory experiments that show that high-frequency radiation lies in part in the off-fault coseismic damage propagating behind the rupture front (Marty et al., 2019), as well as with numerical studies using pre-existing short branches (X. Ma & Elbanna, 2019) or damage-breakage rheology (Mia, Zhao, et al., 2024). Furthermore, the high-frequency content increases with depth, as shown by a shift of the frequency plateau toward higher frequencies and in agreement with natural observations. This trend is attributed to the systematic decrease in branch size with increasing depth. In cases with an initial exponential decay of damage, these features are maintained, if not more pronounced (Figure S7 in Supporting Information S1).

## 5. Discussion and Conclusion

We have investigated the evolution of the damage zone with depth using a numerical model that incorporates the dependence of fracture toughness on loading rate and crack-tip velocities. Our findings reveal that while the width of the damage zone decreases with depth, exhibiting a funnel-shaped structure correlated with the reduction of the process zone size, its density concurrently increases. Despite the relatively narrow width of the damage zone, its influence on rupture dynamics remains significant at all depths as all processes occur at the scale of the process zone. Similar findings have been discussed by Mia et al. (2022). In the presence of damage, the slip rate remains relatively constant, effectively preventing the emergence of nonphysical values of slip rates observed in the elastic case. The high-frequency content of the slip rate is enhanced by damage and depth. Additionally, damage slows down the rupture speed at all depths and can even prevent or delay the transition to supershear.

Simulations are primarily conducted in 2D, but a more comprehensive investigation of 3D effects is necessary. These 3D effects are expected to be significant at shallow depths, with their influence diminishing substantially as depth increases. This has been partially explored by S. Ma (2008), where they compared 3D simulations to their 2D counterparts using Drucker-Prager plasticity. As shown in Figure 3 of their study, the 3D effects are pronounced at shallow depths but become negligible deeper.

To properly assess the damage zone strong influence on rupture dynamics, one should compute the energy budget to quantitatively measure the bulk energetic dissipation due to off-fault crack growth. This work is currently under development. Geophysical observations also suggest a gradual recovery of the elastic properties after an earthquake due to healing processes. Thus the bulk is constantly evolving during the co- and inter-seismic periods, and so is the quantity of energy stored and dissipated in the medium. The structure of the damage zone has also an impact on the permeability, hence on the fluid flow and consequently on the fault resistance to slip. An increase of permeability can also favor aseismic sliding by pressure-solution, which may play significant role in accommodating the afterslip recorded after large earthquakes. This can be followed by a transition back to seismic behavior due to compaction by pressure-solution (den Hartog et al., 2012). The cumulative picture from these studies suggests that on top of the “seismic cycle” there is a superimposed “cycle” where the slip dynamics impact the bulk evolution, which in turn influences back the fault motion. Meyer et al. (2024) proposed, based on experimental analysis, that off-fault deformation can induce unstable slip by decreasing the stiffness of the surrounding rock volume. They emphasized that earthquakes are inherently volumetric processes and observed recurring cycles of localization and delocalization during a series of stick-slip events. This intertwined dynamic should be explored in numerical model to determine its impact on the full seismic cycle. Our model only allows to simulate a single rupture and not the full seismic cycle. Therefore, as a proof of concept, we have implemented a simple 1D spring-slider model with rate and state friction to simulate fault slip over several seismic cycles. The implementation allows for normal stress variations to reproduce changes of the load in the bulk such as seasonal hydrological loading or tides as well as bulk elastic properties variations in the form of varying spring stiffness (implementation details in SM). The adjustments in bulk elastic properties are designed to reflect earthquake-related off-fault damage and healing processes, as documented both in natural fault zones and laboratory experiments (Niu et al., 2008; Shreedharan et al., 2020; Vidale & Li, 2003).

We compare results (Figure 8) of a reference model where the bulk properties stay constant—both normal stress and spring stiffness constant (C0)—with two other models: one with normal stress variations only (C1) and another one with normal stress and stiffness variations (C2). In the absence of normal stress and stiffness variations (C0), the system reaches a perfectly periodic steady-state with regular earthquakes having consistent slip velocities. In model C1, sinusoidal variations in normal stress, stemming from pore pressure fluctuations, disrupt the periodicity, yet the slip velocities remain constant. These variations in pore pressure alter the effective normal stress, consequently affecting the resistance to motion and the timing of events. In C2, with both sinusoidal normal stress and stiffness variations, events become non-periodic, varying in slip velocity by several orders of magnitude. Slow slip events (SSEs) occur alongside regular earthquakes, challenging the common notion that frictional properties variations drive SSEs. Instead, in this model SSEs are attributed to a co-temporal evolution of stiffness and effective normal stress, influenced by what, in nature, would be crack healing-induced changes in bulk elastic properties, permeability, and effective normal stress. Mia et al. (2023) also observed a spectrum of slip depending on the bulk material strength, using an elastoplastic spring-slider model.

This phenomena can be explained as follows. The critical nucleation size  $L_c$ , the minimum size for an instability to grow, is linked to a critical stiffness  $k_c$  that depends on frictional parameters ( $a$ ,  $b$  and  $D_c$ ) and effective normal stress  $\sigma_{eff}$  as:

$$k_c = \left| \frac{\sigma_{eff}(b-a)}{D_c} \right|. \quad (12)$$

Without frictional properties variations—as in our case— $L_c$  solely depends on  $\sigma_{eff}$  and  $k$  which vary over time. Thus, within this simple 1D system, the nucleation length is sometimes small enough that an instability can grow and triggers seismic velocity while sometimes it cannot reach dynamic values.

This analysis still holds for Earth's case. The stiffness  $k$  can be related to elastic rock properties as follows:

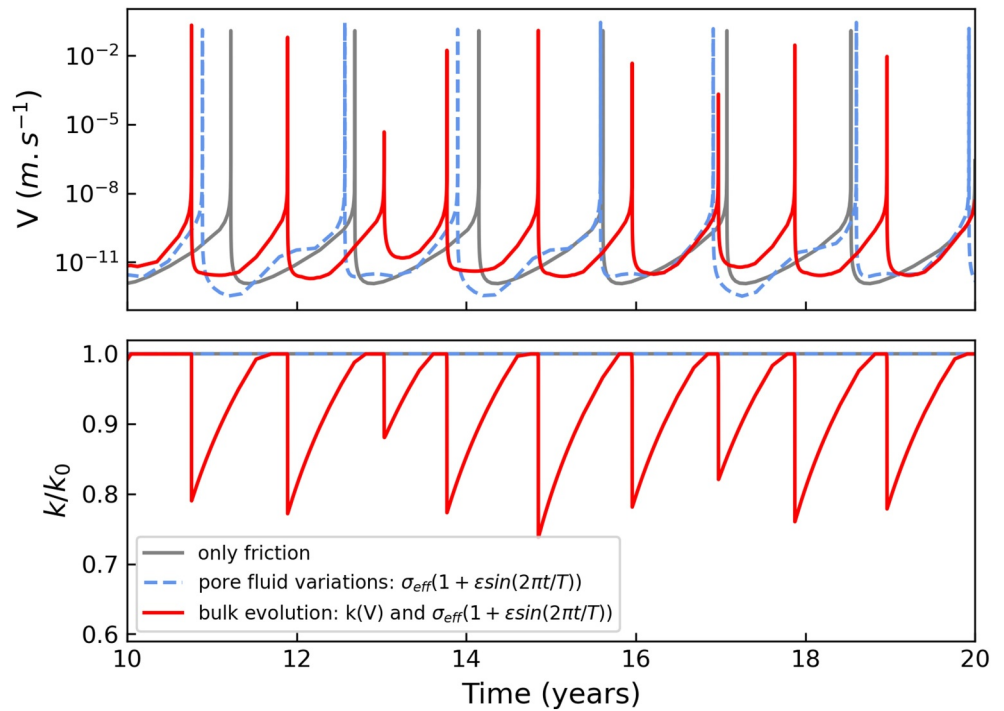


**Figure 8.** Comparison between cases C0, C1 and C2. C0: friction only, both normal stress and stiffness are constant (gray). C1: normal stress variation only (dashed blue). C2: normal stress and stiffness variations (red). Upper part: slip velocity as a function of time. Lower part: stiffness  $k$  normalized by the initial stiffness  $k_0$  as a function of time.

$$k = \frac{\mu}{(1-\nu)L}. \quad (13)$$

Then, for a slipping elliptical patch of fault length  $L$  we have:

$$L_c = \left| \frac{\mu D_c}{(1-\nu)\sigma_{eff}(b-a)} \right|. \quad (14)$$

Slow slip events are explained, both in this study and in the prevailing modeling strategies, as aborted earthquake due to critical nucleation size increase. However, we differ in the suggested mechanisms behind this increase. The prevailing mechanism proposed is frictional parameters changes in which slow slip events occur on patches close to velocity neutral ( $b - a \approx 0$ , hence  $L_c \rightarrow \infty$ ) while we argue that the evolution of the bulk induced by crack growth and healing, which has been abundantly observed in the field is a sufficient (and more likely?) explanation for the fault slip spectrum as observed by geodesy and seismology. Thakur and Huang (2024) have conducted a comprehensive study modeling the damage zone throughout the entire seismic cycle. They modeled the damage zone as a homogeneous elastic layer surrounding the fault plane, with a lower shear modulus compared to the embedding medium (30% reduction). Upon the initiation of coseismic slip, they applied an additional slight decrease (0.5%) in the shear modulus, followed by a logarithmic healing process gradually restoring it to its original value over time. Their findings revealed a broad spectrum of fault slip behavior. However, they introduced friction parameter variations along the dip, unlike our 1D model, where friction remains constant. This disparity underscores that, in our scenario, it is indeed the bulk properties that dictate the response, rather than variations in friction. Although their model does not incorporate a true feedback between the bulk and the fault plane, it represents the right step toward integrating bulk evolution into seismic cycle modeling.

### Data Availability Statement

All the necessary data to reproduce the results are available on Zenodo (Ferry, 2024).

**Acknowledgments**

This study was supported by the Agence National de la Recherche (ANR) IDEAS contract ANR-19-CE31-0004-01. The computations presented here were conducted on the MADARIAGA cluster supported by the European Research Council grant PERSISMO (Grant 865411).

**References**

Ampuero, J.-P. (2012). SEM2DPACK, a spectral element software for 2D seismic wave propagation and earthquake source dynamics. <https://doi.org/10.5281/zenodo.230363>

Andrews, D. J. (1976). Rupture velocity of plane strain shear cracks. *Journal of Geophysical Research*, *81*(32), 5679–5687. <https://doi.org/10.1029/JB081i032p05679>

Andrews, D. J. (2005). Rupture dynamics with energy loss outside the slip zone. *Journal of Geophysical Research*, *110*(B1). <https://doi.org/10.1029/2004JB003191>

Barnes, P. M., Wallace, L. M., Saffer, D. M., Bell, R. E., Underwood, M. B., Fagereng, A., et al. (2020). Slow slip source characterized by lithological and geometric heterogeneity. *Science Advances*, *6*(13). <https://doi.org/10.1126/sciadv.aay3314>

Bedford, J. D., Faulkner, D. R., & Lapusta, N. (2022). Fault rock heterogeneity can produce fault weakness and reduce fault stability. *Nature Communications*, *13*(1), 326. <https://doi.org/10.1038/s41467-022-27998-2>

Ben-Zion, Y., & Ampuero, J.-P. (2009). Seismic radiation from regions sustaining material damage. *Geophysical Journal International*, *178*(3), 1351–1356. <https://doi.org/10.1111/j.1365-246X.2009.04285.x>

Bhat, H. S., Rosakis, A. J., & Sammis, C. G. (2012). A micromechanics based constitutive model for brittle failure at high strain rates. *Journal of Applied Mechanics*, *79*(3), 031016. <https://doi.org/10.1115/1.4005897>

Brantut, N., Heap, M. J., Meredith, P. G., & Baud, P. (2013). Time-dependent cracking and brittle creep in crustal rocks: A review. *Journal of Structural Geology*, *52*, 17–43. <https://doi.org/10.1016/j.jsg.2013.03.007>

Brenguier, F., Campillo, M., Hadziioannou, C., Shapiro, N. M., Nadeau, R. M., & Larose, E. (2008). Postseismic relaxation along the San Andreas fault at Parkfield from continuous seismological observations. *Science*, *321*(5895), 1478–1481. <https://doi.org/10.1126/science.1160943>

Cochran, E. S., Li, Y.-G., Shearer, P. M., Barbot, S., Fialko, Y., & Vidale, J. E. (2009). Seismic and geodetic evidence for extensive, long-lived fault damage zones. *Geology*, *37*(4), 315–318. <https://doi.org/10.1130/G25306A.1>

den Hartog, S. A. M., Peach, C. J., de Winter, D. A. M., Spiers, C. J., & Shimamoto, T. (2012). Frictional properties of megathrust fault gouges at low sliding velocities: New data on effects of normal stress and temperature. *Journal of Structural Geology*, *38*, 156–171. <https://doi.org/10.1016/j.jsg.2011.12.001>

Faulkner, D. R., Mitchell, T. M., Healy, D., & Heap, M. J. (2006). Slip on “weak” faults by the rotation of regional stress in the fracture damage zone. *Nature*, *444*(7121), 922–925. <https://doi.org/10.1038/nature05353>

Faulkner, D. R., Mitchell, T. M., Jensen, E., & Cembrano, J. (2011). Scaling of fault damage zones with displacement and the implications for fault growth processes. *Journal of Geophysical Research*, *116*(B5), B05403. <https://doi.org/10.1029/2010JB007788>

Ferry. (2024). Simulations for “depth dependence of coseismic off-fault damage and its effects on rupture dynamics” [Dataset]. *Zenodo*. <https://doi.org/10.5281/zenodo.14013715>

Froment, B., McGuire, J. J., van der Hilst, R. D., Gouédard, P., Roland, E. C., Zhang, H., & Collins, J. A. (2014). Imaging along-strike variations in mechanical properties of the Gofar transform fault, East Pacific Rise. *Journal of Geophysical Research: Solid Earth*, *119*(9), 7175–7194. <https://doi.org/10.1002/2014JB011270>

Gao, G., Yao, W., Xia, K., & Li, Z. (2015). Investigation of the rate dependence of fracture propagation in rocks using digital image correlation (DIC) method. *Engineering Fracture Mechanics*, *138*, 146–155. <https://doi.org/10.1016/j.engfracmech.2015.02.021>

Jandert Ribes, L., Thomas, M. Y., & Bhat, H. S. (2023). On the importance of setting 3-D stress field in simulations of on- and off-fault deformation. *Geophysical Journal International*, *235*(3), 2962–2978. <https://doi.org/10.1093/gji/ggad401>

Johnson, S. E., Song, W. J., Vel, S. S., Song, B. R., & Gerbi, C. C. (2021). Energy partitioning, dynamic fragmentation, and off-fault damage in the earthquake source volume. *Journal of Geophysical Research: Solid Earth*, *126*(11), e2021JB022616. <https://doi.org/10.1029/2021JB022616>

Ma, S. (2008). A physical model for widespread near-surface and fault zone damage induced by earthquakes. *Geochemistry, Geophysics, Geosystems*, *9*(11). <https://doi.org/10.1029/2008GC002231>

Ma, X., & Elbanna, A. (2019). Dynamic rupture propagation on fault planes with explicit representation of short branches. *Earth and Planetary Science Letters*, *523*, 115702. <https://doi.org/10.1016/j.epsl.2019.07.005>

Marty, S., Passelègue, F. X., Aubry, J., Bhat, H. S., Schubnel, A., & Madariaga, R. (2019). Origin of high-frequency radiation during laboratory earthquakes. *Geophysical Research Letters*, *46*(7), 3755–3763. <https://doi.org/10.1029/2018GL080519>

Meyer, G. G., Giorgetti, C., Guérin-Marthe, S., & Violay, M. (2024). Off-fault deformation feedback and strain localization precursor during laboratory earthquakes. *Communications Earth & Environment*, *5*(1), 1–7. <https://doi.org/10.1038/s43247-024-01756-2>

Mia, M. S., Abdelmeguid, M., & Elbanna, A. E. (2022). Spatio-temporal clustering of seismicity enabled by off-fault plasticity. *Geophysical Research Letters*, *49*(8), e2021GL097601. <https://doi.org/10.1029/2021GL097601>

Mia, M. S., Abdelmeguid, M., & Elbanna, A. E. (2023). The spectrum of fault slip in elastoplastic fault zones. *Earth and Planetary Science Letters*, *619*, 118310. <https://doi.org/10.1016/j.epsl.2023.118310>

Mia, M. S., Abdelmeguid, M., Harris, R. A., & Elbanna, A. E. (2024). Rupture jumping and seismic complexity in models of earthquake cycles for fault stepovers with off-fault plasticity. *Bulletin of the Seismological Society of America*, *114*(3), 1466–1480. <https://doi.org/10.1785/0120230249>

Mia, M. S., Zhao, C., Elbanna, A., & Ben-Zion, Y. (2024). Dynamic rupture modeling in a complex fault zone with distributed and localized damage. *Mechanics of Materials*, *198*, 105139. <https://doi.org/10.1016/j.mechmat.2024.105139>

Mitchell, T. M., & Faulkner, D. R. (2008). Experimental measurements of permeability evolution during triaxial compression of initially intact crystalline rocks and implications for fluid flow in fault zones. *Journal of Geophysical Research*, *113*(B11). <https://doi.org/10.1029/2008JB005588>

Mitchell, T. M., & Faulkner, D. R. (2009). The nature and origin of off-fault damage surrounding strike-slip fault zones with a wide range of displacements: A field study from the Atacama fault system, northern Chile. *Journal of Structural Geology*, *31*(8), 802–816. <https://doi.org/10.1016/j.jsg.2009.05.002>

Mitchell, T. M., & Faulkner, D. R. (2012). Towards quantifying the matrix permeability of fault damage zones in low porosity rocks. *Earth and Planetary Science Letters*, *339–340*, 24–31. <https://doi.org/10.1016/j.epsl.2012.05.014>

Morad, D., Sagy, A., Tal, Y., & Hatzor, Y. H. (2022). Fault roughness controls sliding instability. *Earth and Planetary Science Letters*, *579*, 117365. <https://doi.org/10.1016/j.epsl.2022.117365>

Niu, F., Silver, P. G., Daley, T. M., Cheng, X., & Majer, E. L. (2008). Preseismic velocity changes observed from active source monitoring at the Parkfield SAFOD drill site. *Nature*, *454*(7201), 204–208. <https://doi.org/10.1038/nature07111>

Okubo, K., Bhat, H. S., Rougier, E., Marty, S., Schubnel, A., Lei, Z., et al. (2019). Dynamics, radiation, and overall energy budget of earthquake rupture with coseismic off-fault damage. *Journal of Geophysical Research: Solid Earth*, *124*(11), 11771–11801. <https://doi.org/10.1029/2019JB017304>

- Okubo, K., Esteban, R., Zhou, L., & Bhat, H. S. (2020). Modeling earthquakes with off-fault damage using the combined finite-discrete element method. *Journal of Geophysical Research: Solid Earth*, *125*(1), 1057–1072. <https://doi.org/10.1007/s40571-020-00335-4>
- Palgunadi, K. H., Gabriel, A.-A., Garagash, D. I., Ulrich, T., & Mai, P. M. (2024). Rupture dynamics of cascading earthquakes in a multiscale fracture network. *Journal of Geophysical Research: Solid Earth*, *129*(3). <https://doi.org/10.1029/2023JB027578>
- Palmer, A. C., Rice, J. R., & Hill, R. (1973). The growth of slip surfaces in the progressive failure of over-consolidated clay. *Proceedings of the Royal Society of London. A. Mathematical and Physical Sciences*, *332*(1591). <https://doi.org/10.1098/rspa.1973.0040>
- Perrin, C., Manighetti, I., Ampuero, J.-P., Cappa, F., & Gaudemer, Y. (2016). Location of largest earthquake slip and fast rupture controlled by along-strike change in fault structural maturity due to fault growth. *Journal of Geophysical Research: Solid Earth*, *121*(5), 3666–3685. <https://doi.org/10.1002/2015JB012671>
- Pio Lucente, F., De Gori, P., Margheriti, L., Piccinini, D., Di Bona, M., Chiarabba, C., & Piana Agostinetti, N. (2010). Temporal variation of seismic velocity and anisotropy before the 2009 MW 6.3 L'Aquila earthquake, Italy. *Geology*, *38*(11), 1015–1018. <https://doi.org/10.1130/G31463.1>
- Poliakov, A. N. B., Dmowska, R., & Rice, J. R. (2002). Dynamic shear rupture interactions with fault bends and off-axis secondary faulting. *Journal of Geophysical Research*, *107*(B11). <https://doi.org/10.1029/2001JB000572>
- Qiu, H., Ben-Zion, Y., Catchings, R., Goldman, M. R., Allam, A. A., & Steidl, J. (2021). Seismic imaging of the Mw 7.1 ridgecrest earthquake rupture zone from data recorded by dense linear arrays. *Journal of Geophysical Research: Solid Earth*, *126*(7). <https://doi.org/10.1029/2021JB022043>
- Rice, J. R. (1971). Inelastic constitutive relations for solids: An internal-variable theory and its application to metal plasticity. *Journal of the Mechanics and Physics of Solids*, *19*(6), 433–455. [https://doi.org/10.1016/0022-5096\(71\)90010-X](https://doi.org/10.1016/0022-5096(71)90010-X)
- Rice, J. R., Sammis, C. G., & Parsons, R. (2005). Off-fault secondary failure induced by a dynamic slip pulse. *Bulletin of the Seismological Society of America*, *95*(1), 109–134. <https://doi.org/10.1785/0120030166>
- Rodríguez Padilla, A. M., Oskin, M. E., Milliner, C. W. D., & Plesch, A. (2022). Accrual of widespread rock damage from the 2019 Ridgecrest earthquakes. *Nature Geoscience*, *15*(3), 222–226. <https://doi.org/10.1038/s41561-021-00888-w>
- Romanet, P., Bhat, H. S., Jolivet, R., & Madariaga, R. (2018). Fast and slow slip events emerge due to fault geometrical complexity. *Geophysical Research Letters*, *45*(10), 4809–4819. <https://doi.org/10.1029/2018GL077579>
- Savage, H. M., & Brodsky, E. E. (2011). Collateral damage: Evolution with displacement of fracture distribution and secondary fault strands in fault damage zones. *Journal of Geophysical Research*, *116*(B3), B03405. <https://doi.org/10.1029/2010JB007665>
- Shreedharan, S., Bolton, D. C., Rivière, J., & Marone, C. (2020). Preseismic fault creep and elastic wave amplitude precursors scale with lab earthquake magnitude for the continuum of tectonic failure modes. *Geophysical Research Letters*, *47*(8). <https://doi.org/10.1029/2020GL086986>
- Thakur, P., & Huang, Y. (2024). The effects of precursory velocity changes on earthquake nucleation and stress evolution in dynamic earthquake cycle simulations. *Earth and Planetary Science Letters*, *637*, 118727. <https://doi.org/10.1016/j.epsl.2024.118727>
- Thomas, M. Y., & Bhat, H. S. (2018). Dynamic evolution of off-fault medium during an earthquake: A micromechanics based model. *Geophysical Journal International*, *214*(2), 1267–1280. <https://doi.org/10.1093/gji/ggy129>
- Thomas, M. Y., Bhat, H. S., & Klinger, Y. (2017). Effect of brittle off-fault damage on earthquake rupture dynamics. In *Fault zone dynamic processes* (pp. 255–280). American Geophysical Union (AGU).
- Vermilye, J. M., & Scholz, C. H. (1998). The process zone: A microstructural view of fault growth. *Journal of Geophysical Research*, *103*(B6), 12223–12237. <https://doi.org/10.1029/98JB00957>
- Vidale, J. E., & Li, Y.-G. (2003). Damage to the shallow Landers fault from the nearby Hector Mine earthquake. *Nature*, *421*(6922), 524–526. (Publisher: Nature Publishing Group). <https://doi.org/10.1038/nature01354>
- Wang, Q. Z., Feng, F., Ni, M., & Gou, X. P. (2011). Measurement of mode I and mode II rock dynamic fracture toughness with cracked straight through flattened Brazilian disc impacted by split Hopkinson pressure bar. *Engineering Fracture Mechanics*, *78*(12), 2455–2469. <https://doi.org/10.1016/j.engfracmech.2011.06.004>
- Wilson, J. E., Chester, J. S., & Chester, F. M. (2003). Microfracture analysis of fault growth and wear processes, Punchbowl Fault, San Andreas system, California. *Journal of Structural Geology*, *25*(11), 1855–1873. [https://doi.org/10.1016/S0191-8141\(03\)00036-1](https://doi.org/10.1016/S0191-8141(03)00036-1)
- Xu, S., Fukuyama, E., Yamashita, F., Kawakata, H., Mizoguchi, K., & Takizawa, S. (2023). Fault strength and rupture process controlled by fault surface topography. *Nature Geoscience*, *16*(1), 94–100. <https://doi.org/10.1038/s41561-022-01093-z>
- Zhang, Q. B., & Zhao, J. (2013). Effect of loading rate on fracture toughness and failure micromechanisms in marble. *Engineering Fracture Mechanics*, *102*, 288–309. <https://doi.org/10.1016/j.engfracmech.2013.02.009>

## References From the Supporting Information

- Perfettini, H., Schmittbuhl, J., Rice, J. R., & Cocco, M. (2001). Frictional response induced by time-dependent fluctuations of the normal loading. *Journal of Geophysical Research*, *106*(B7), 13455–13472. <https://doi.org/10.1029/2000JB900366>
- Ruina, A. (1983). Slip instability and state variable friction laws. *Journal of Geophysical Research*, *88*(B12), 10359–10370. <https://doi.org/10.1029/JB088iB12p10359>

# Supporting Information for ”Depth Dependence of Coseismic Off-Fault Damage and its Effects on Rupture Dynamics”

Roxane Ferry<sup>1</sup>, Marion Y. Thomas<sup>2</sup>, Harsha S. Bhat <sup>3</sup>, Pierpaolo Dubernet<sup>3</sup>

<sup>1</sup>Institute of Civil Engineering, Institute of Materials Science and Engineering, École Polytechnique Fédérale de Lausanne (EPFL),

Lausanne, Switzerland

<sup>2</sup>Institut des Sciences de la Terre de Paris, Sorbonne Université, CNRS, UMR 7193, Paris, France

<sup>3</sup>Laboratoire de Géologie, Département de Géosciences, École Normale Supérieure, CNRS, UMR 8538, PSL Université, Paris, France

## Content

This document contains

1. Details on the spring-slider with normal stress and stiffness variations derivation and implementation.

2. Additional figures:

- S1: Comparison of damage states without non-dimensionalization at 2, 6 and 10 km depth.

- S2: Comparison of damage states for simulations with an initial damage decreasing exponentially from the fault.



- S3: Comparison of damage zone width for an initial homogeneous damage state and for an initial exponential damage.

- S4: Comparison of cumulative slip for the elastic and damage cases.

- S5: Comparison of slip rate for the elastic and damage cases.

- S6: Comparison of rupture front locations and peak velocity for elastic, homogeneous initial damage state and exponentially decreasing initial damage cases.

- S7: Comparison of Fourier amplitude spectra of slip rate for the cases with an initial exponentially decreasing damage state.

## Spring-slider with normal stress and stiffness variations

We have implemented the spring-slider model with varying normal stress described in Perfettini, Schmittbuhl, Rice, and Cocco (2001). This model enables us to replicate variations in load within the bulk, such as seasonal hydrological loading or tides. To simulate variations in bulk elastic properties, we incorporate varying spring stiffness into the aforementioned model.

### Governing equations

A spring-slider is a simple model where a rigid block connected to a spring of stiffness  $k$  is pulled at a constant velocity  $V_0$ . Friction is governed by a rate-and-state friction which in Perfettini et al. (2001) takes the following form (Ruina, 1983):

$$\tau = \sigma \left( \mu_0 + a \ln \left( \frac{V}{V_*} \right) + \psi \right), \quad (1)$$

with  $V_*$  a normalizing velocity and  $\psi$  a state variable whose derivative is given by:

$$\frac{d\psi}{dt} = -\frac{V}{D_c} \left( \psi + b \ln \left( \frac{V}{V_*} \right) \right) - \frac{\alpha}{\sigma} \frac{d\sigma}{dt}. \quad (2)$$

$\alpha$  is a normal stress variation coefficient between 0 and  $\mu_0$  (see Perfettini et al. (2001) for details). This rate-and-state formulation features a varying normal stress  $\sigma(t)$  which is expressed as:

$$\sigma(t) = \sigma_0 (1 + \epsilon f(t)), \quad |\epsilon f(t)| \ll 1. \quad (3)$$

The two forces at work are the spring restoring force and friction. Hence applying Newton's second law gives:

$$m \frac{dV}{dt} = ku - \tau, \quad (4)$$

with  $u$  the spring displacement and  $\dot{u} = V_0 - V$ . We approximate the system by saying  $m = 0$  and add a radiation damping term  $\eta V$ . Eq. (4) then becomes:

$$\tau = ku - \eta V, \quad (5)$$

with  $\eta = \mu/(2c_s)$  and  $c_s$  the shear wave velocity. Eq. (1) and Eq. (5) are equal. Differentiating them with respect to time one gets:

$$\frac{dV}{dt} = \left[ \frac{dk}{dt} u + k(V_0 - V) - \left( \mu_0 + a \ln \left( \frac{V}{V_*} \right) + \psi \right) \frac{d\sigma}{dt} - \sigma \frac{d\psi}{dt} \right] / \left[ \frac{a}{V} \sigma + \eta \right]. \quad (6)$$

Finally, the system of ordinary differential equations is:

$$\begin{cases} \frac{du}{dt} = V_0 - V \\ \frac{d\psi}{dt} = -\frac{V}{D_c} \left( \psi + b \ln \left( \frac{V}{V_*} \right) \right) - \frac{\alpha}{\sigma} \frac{d\sigma}{dt} \\ \frac{dV}{dt} = \left[ \frac{dk}{dt} u + k(V_0 - V) - \left( \mu_0 + a \ln \left( \frac{V}{V_*} \right) + \psi \right) \frac{d\sigma}{dt} - \sigma \frac{d\psi}{dt} \right] / \left[ \frac{a}{V} \sigma + \eta \right]. \end{cases} \quad (7)$$

### Spring stiffness variations

Spring stiffness  $k$  is the equivalent in our 1D system of the bulk elastic properties. Therefore, we use geologic and geodetic observations to set its evolution. A drop in seismic velocities followed by a partial recovery is observed after an earthquake (Froment et al., 2014) and attributed to elastic properties changes due to damage. In our model,  $k$  follows a law that reproduces this behaviour. Inspired by shape-similarity between seismic velocities evolution (Froment et al., 2014) and friction coefficient evolution after a change in loading velocity, we define a velocity-dependent evolution law for  $k$  similar to the rate-and-state law with a state variable  $\theta_k$  for the spring. We thus have:

$$k(t) = k_0 \left( 1 + b_k \ln \left( \frac{V_0 \theta_k}{D_k} \right) \right) \quad (8)$$

and:

$$\frac{d\theta_k}{dt} = 1 - \frac{V\theta_k}{D_k}, \quad (9)$$

with  $k_0$  the initial spring stiffness. This differential equation is joined to Eq. (7) to form the governing system:

$$\begin{cases} \frac{du}{dt} = V_0 - V \\ \frac{d\psi}{dt} = -\frac{V}{D_c} \left( \psi + b \ln \left( \frac{V}{V_*} \right) \right) - \frac{\alpha}{\sigma} \frac{d\sigma}{dt} \\ \frac{dV}{dt} = \left[ \frac{dk}{dt} u + k (V_0 - V) - \left( \mu_0 + a \ln \left( \frac{V}{V_*} \right) + \psi \right) \frac{d\sigma}{dt} - \sigma \frac{d\psi}{dt} \right] / \left[ \frac{a}{V} \sigma + \eta \right] \\ \frac{d\theta_k}{dt} = 1 - \frac{V\theta_k}{D_k}. \end{cases} \quad (10)$$

This system is solved using a Bulirsch-Stoer method with adaptive time-stepping. It allows a fine temporal resolution when needed while staying computationally efficient.

## Settings

In this spring-slider model, the seismic velocity drop after an earthquake depends on the parameter  $b_k$ . Therefore, we set  $b_k$  value to reproduce drop amounts observed by Froment et al. (2014).

The initial spring stiffness  $k_0$  is taken to be a fraction of the critical stiffness  $k_c$  given by  $k_c = \sigma_0(b - a)/D_k$  as the system is unstable if  $k < k_c$ . Normal stress variations are sinusoidal, that is  $f(t)$  in Eq. (3) is equal to  $\sin(2\pi t/T)$  with  $T$  the period. All parameters used are summarized in Table S1.

## References

- Froment, B., McGuire, J. J., van der Hilst, R. D., Gouédard, P., Roland, E. C., Zhang, H., & Collins, J. A. (2014). Imaging along-strike variations in mechanical properties of the Gofar transform fault, East Pacific Rise. *Journal of Geophysical Research: Solid Earth*, *119*(9), 7175–7194. doi: 10.1002/2014JB011270
- Perfettini, H., Schmittbuhl, J., Rice, J. R., & Cocco, M. (2001). Frictional response induced by time-dependent fluctuations of the normal loading. *Journal of Geophysical Research: Solid Earth*, *106*(B7). doi: 10.1029/2000JB900366
- Ruina, A. (1983). Slip instability and state variable friction laws. *Journal of Geophysical Research: Solid Earth*, *88*(B12), 10359–10370. doi: 10.1029/JB088iB12p10359

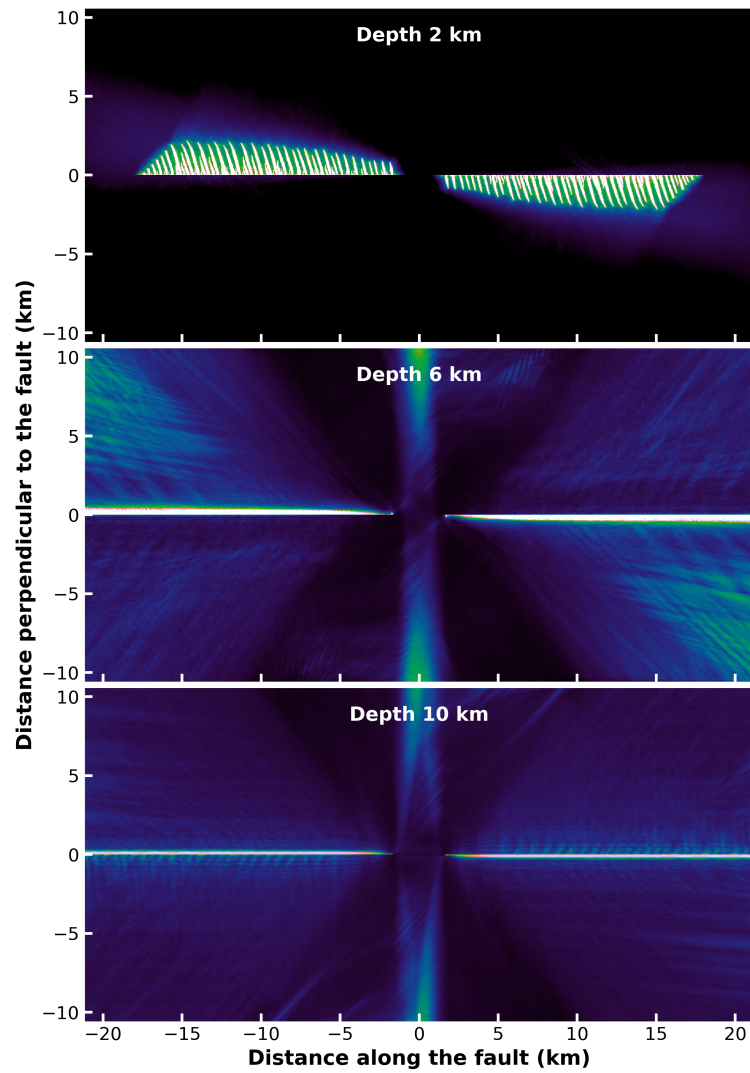


**Figure S1.** Comparison of damage states in simulations at 2, 6 and 10 km without non-dimensionalization. All simulations employ a consistent grid size of 53 m. Hence, there are 20 grid nodes resolving the process zone size at 2 km, while only about 2 and 1 nodes are available for simulations at 6 and 10 km, respectively. This underscores the significance of non-dimensionalization in investigating the evolution of damage states with depth.

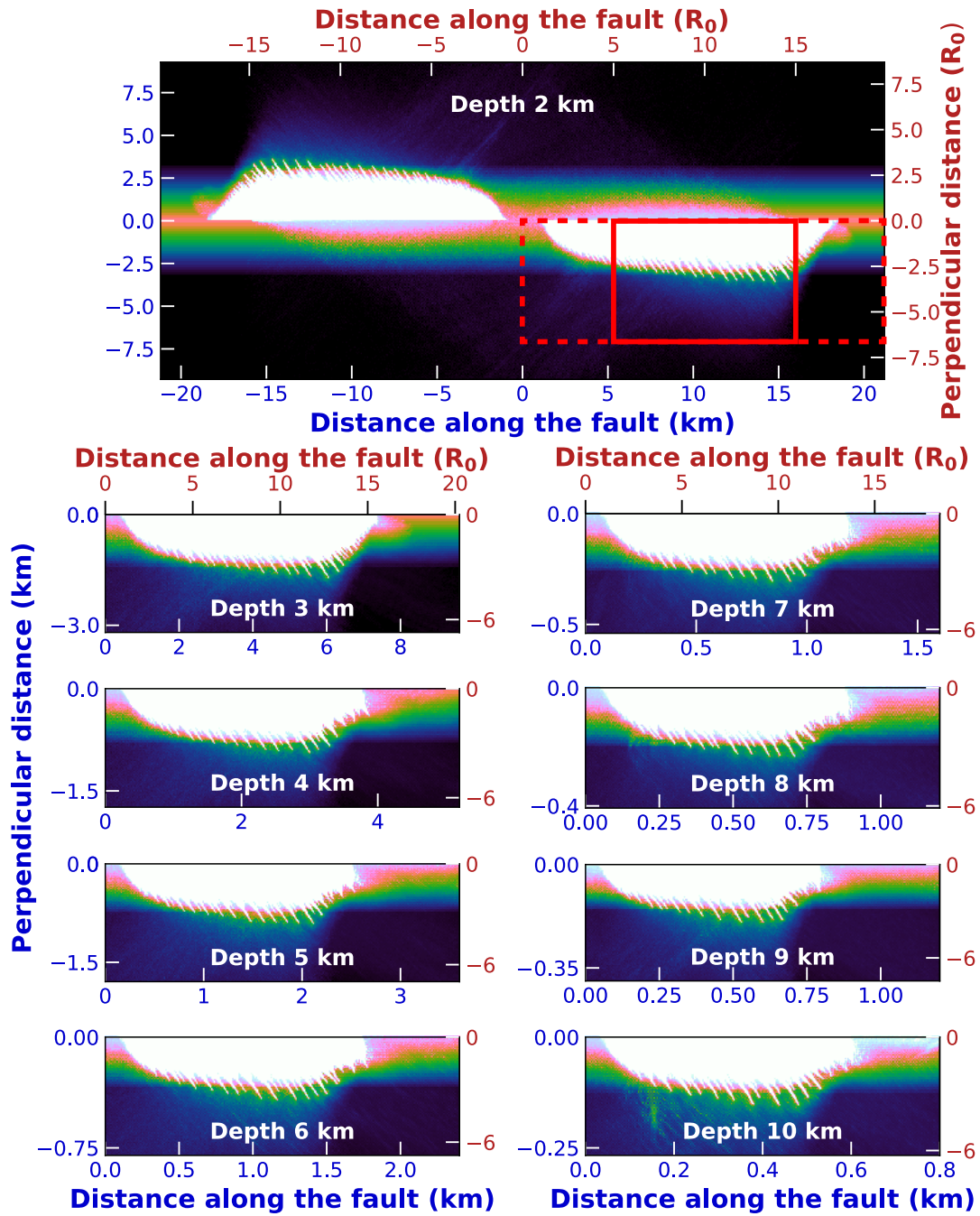


**Figure S2.** Comparison of damage arising from a rupture at depths ranging from 2 to 10 km with an initial damage decreasing exponentially away from the fault. The top panel depicts the entire fault at a depth of 2 km. Given the symmetry of the rupture, the subsequent panels exclusively showcase the bottom-right quadrants (as delimited by the dashed red rectangle in the top panel) of the domain. Both real (km) and non-dimensionalized ( $R_0$ ) distances are given.

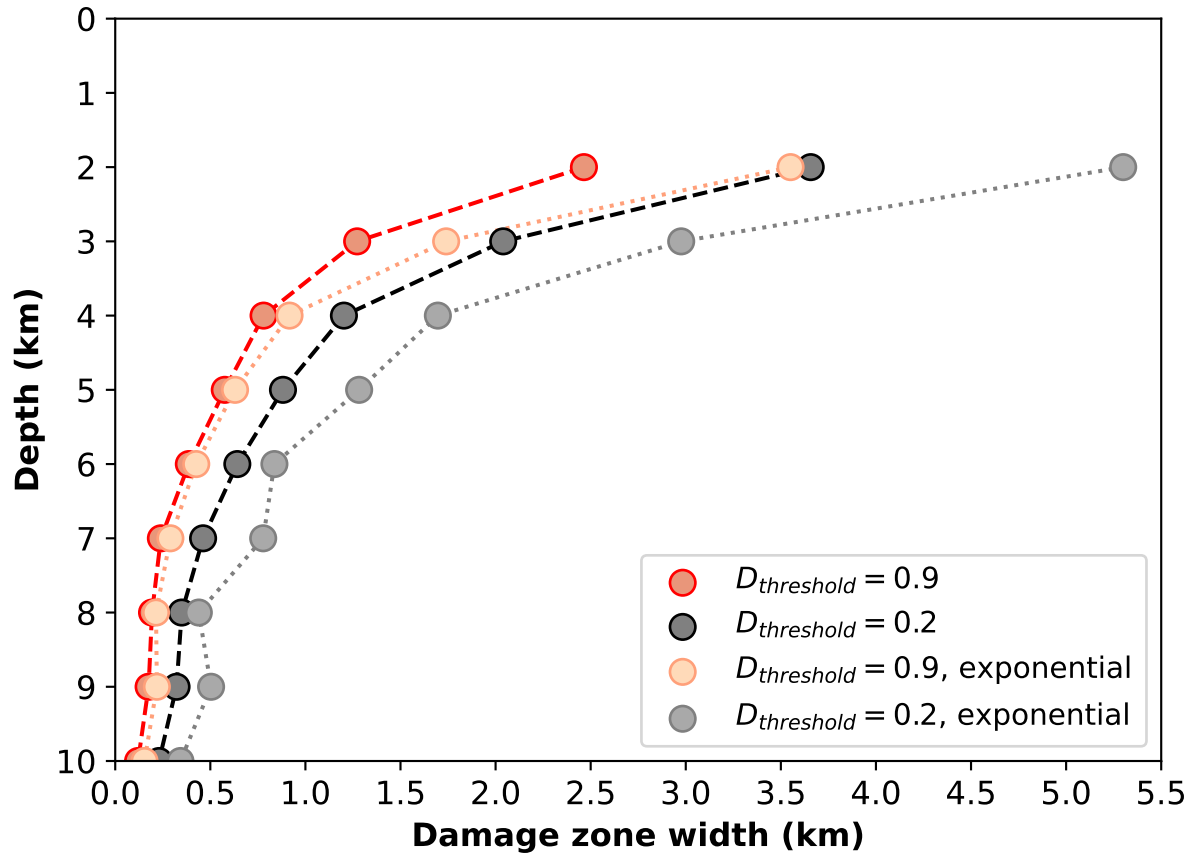


**Figure S3.** Comparison of damage zone width as a function of depth for two distinct damage thresholds for the cases with an initial homogeneous damage state and an initial exponential damage. Both cases display a consistent funnel-shaped structure.



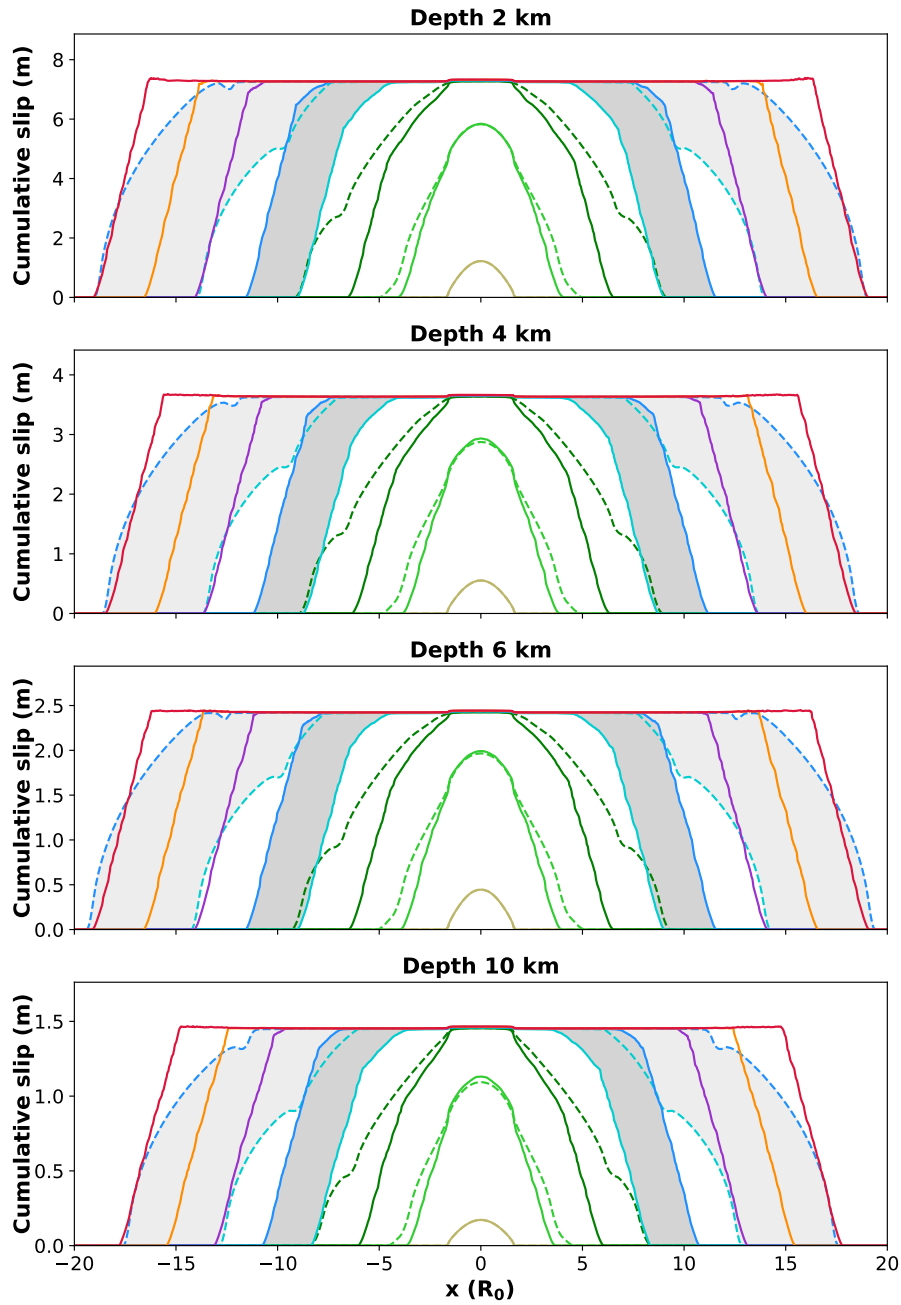


**Figure S4.** Comparison of cumulative slip as a function of distance from the fault center for both the elastic (dashed lines) and damage (continuous lines) cases at different depths. Colors are isochrones, the dark and light gray areas highlight the area that slipped during a given time interval for the damage and elastic case respectively. Both real (km) and non-dimensionalized ( $R_0$ ) distances are given.

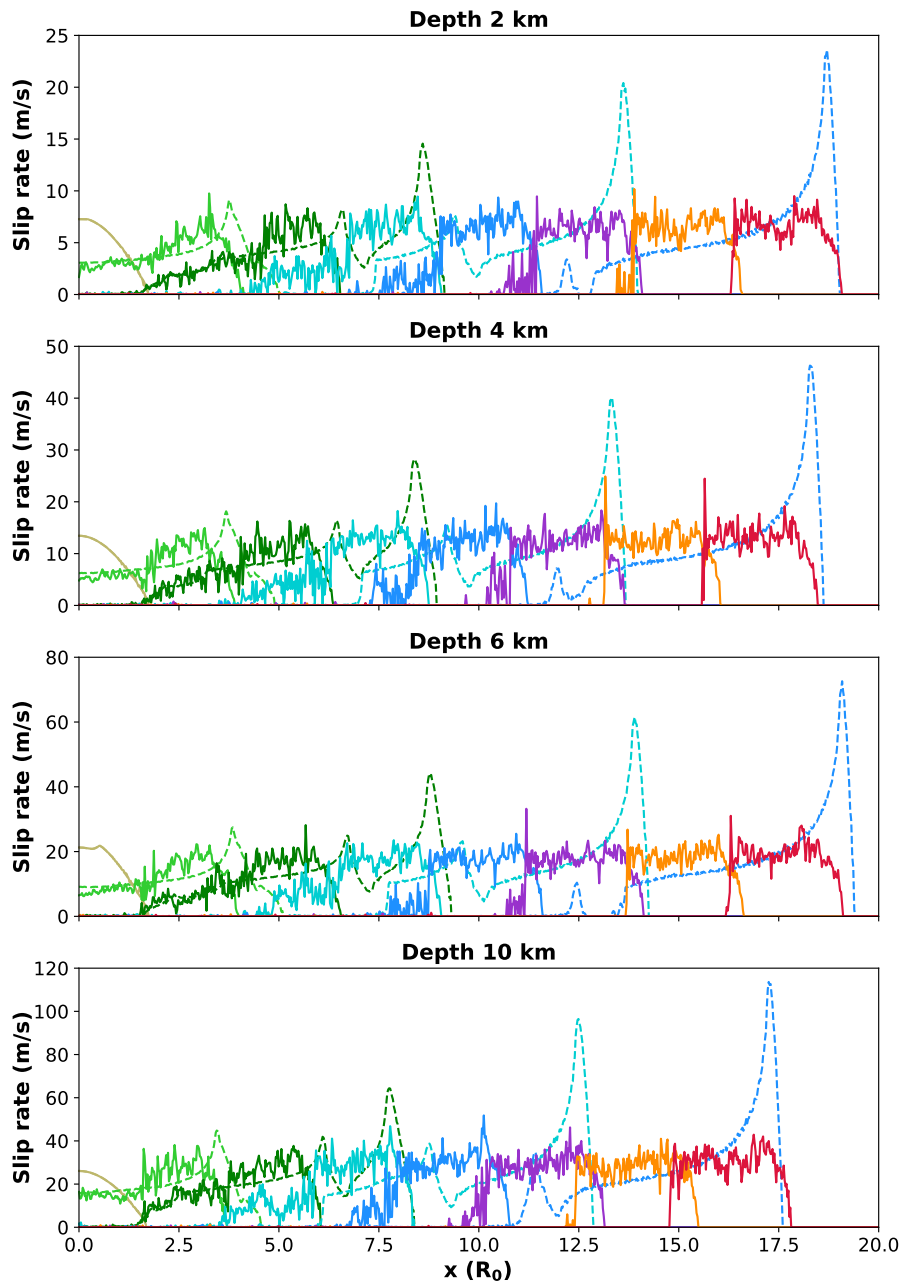


**Figure S5.** Comparison of slip rate as a function of distance from the fault center for both the elastic (dashed lines) and damage (continuous lines) cases at different depths. Colors are isochrones, the dark and light gray areas highlight the area that slipped during a given time interval for the damage and elastic case respectively. Both real (km) and non-dimensionalized ( $R_0$ ) distances are given.

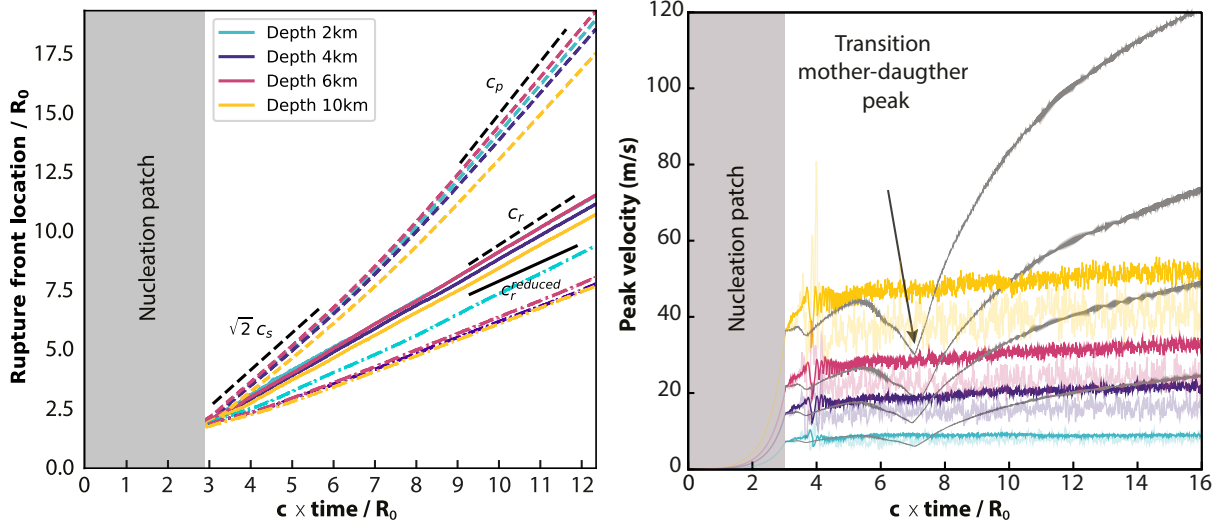


**Figure S6. Left:** Comparison of rupture front locations as a function of dimensionless time at different depths for elastic (dashed lines), homogeneous initial damage state (continuous lines) and exponentially decreasing initial damage (dashed-dotted lines) cases. The black dashed lines indicate for reference the speed domain limits for stable supershear rupture,  $\sqrt{2}c_s$  and  $c_p$ , as well as the upper limit for subshear rupture  $c_r$ , where  $c_s$ ,  $c_p$  and  $c_r$  are respectively the shear, longitudinal and Rayleigh wave speeds. The continuous black line illustrates the reduced Rayleigh wave speed (decreased by 30%) due to damage.

**Right:** Comparison of peak velocity in  $m/s$  as a function of dimensionless time at different depths both for elastic (dashed grey lines) and exponentially decreasing initial damage (continuous lines) cases. The light continuous color lines indicate the homogeneous initial damage case for reference.

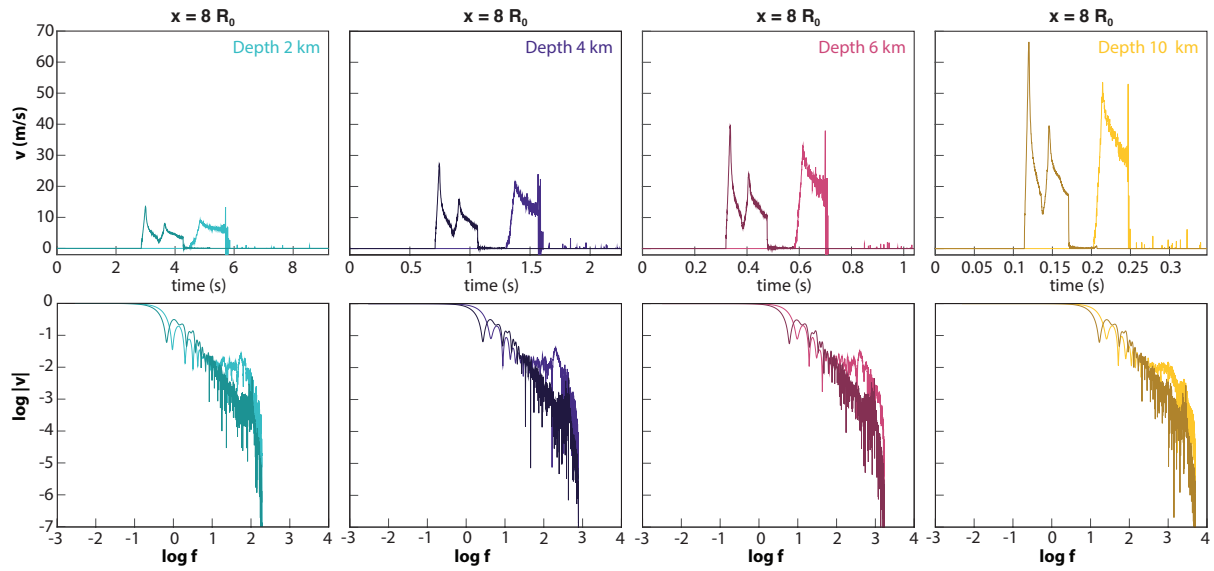


**Figure S7.** Comparison of Fourier amplitude spectra (FAS) of slip rate at different depths for the cases with an initial exponentially decreasing damage state. The dark and light colors correspond to the elastic and damage case respectively.

Symbol	Parameter	Value
$\mu$	Shear modulus	30 MPa
$c_s$	S-wave speed	3500 m/s
$\eta$	Viscous term	$4.3 \times 10^{-6} \text{ kg.m}^{-2}.\text{s}^{-1}$
$\mu_0$	Steady-state friction coefficient	0.6
$a$	R&S friction parameter	0.007
$b$	R&S friction parameter	0.009
$V_*$	Normalizing velocity	$10^{-4} \text{ m/s}$
$D_c$	Critical slip distance	1.35 mm
$\sigma_0$	Mean normal stress	100 MPa
$\alpha$	Normal stress variation coefficient	0.1
$k_c$	Critical spring stiffness	$14.8 \times 10^7 \text{ N/m}$
$k_0$	Initial spring stiffness	$0.95 \times k_c$
$D_k$	Characteristic healing distance	$5 \times 10^{-2} \text{ m}$
$T$	Period of normal stress variation	1 year

**Table S1.** Parameters used for simulations with the spring-slider.